Reconstruction of the Pleistocene Environment and Climate of the Olorgesailie Basin

A Thesis
SUBMITTED TO THE FACULTY OF
UNIVERSITY OF MINNESOTA
BY

Laura M. Cappio

IN PARTIAL FULFILLMENT OF THE REQUIREMENTS
FOR THE DEGREE OF
MASTER OF SCIENCE

Dr. Erik Brown & Dr. Byron Steinman

May 2016

Acknowledgements

First and foremost I wish to acknowledge my thesis advisors, Dr. Erik Brown and Dr. Byron Steinman, for the many opportunities they provided me. Not only was I able to work with scientists from multiple international and interdisciplinary scientific teams on HSPDP, ODP, and MexiDrill, I was also able to travel and work in parts of the world (the Pacific North-West, Alberta, Macedonia, and Mexico City) that I would never have found myself otherwise. I am very grateful for their patience, guidance, support, laughs and tutelage over the past two years. I would also like to thank committee members Mona Stockhecke and John Swenson for their guidance and feedback throughout the course of my project.

Many thanks go to the faculty, staff, and graduate students at the Large Lakes Observatory for their support and company; specifically Virginia Batts, Courtney Targos, Eddie Gazzetti, Dan Titze, Amanda Brennan, Cody Tennant, Aaron Lingwall and Abi Lingwall deserve thanks for keeping me sane and for putting up with my East Coast mouth. I am endlessly grateful for the staff at Memorial Sloan Kettering Hospital for giving me the gifts of peace of mind and more time with my beautiful mother. Special thanks to Lara Brooke Thomas, Faith Carbon, Charlotte Gutfreund, Ali & Jenn Hare, Onika Minaj, Kanye West, and Brandi Carlile.

Last, but certainly not least, I wish to thank my family (Mom, Dad, and Peter) for their unwavering love and support in the face of 1000 miles, culture shock, cancer, single-handedly supporting the airline industry, and past-bedtime phone calls. My love for you three is boundless.

This research project and my academic support were funded through the Smithsonian's Human Origins Project, the Hominin Sites Paleolakes Drilling Project, and the International Continental Scientific Drilling Program.

Abstract

The Smithsonian's Human Origins Program team recovered drill core from the Olorgesailie paleolake in the East African Rift that is likely to contain records of environmental change relevant to hominin evolution. Archeological sites in the Olorgesailie basin show significant innovations in tool use technologies during the mid-late Pleistocene. Core from the Olorgesailie/Koora region has been subject to initial analyses, including XRF scanning. This study focuses on a 10 meter laminated sequence of this core that spans between 100 and 133 meters below the surface. This sequence was not deposited continuously and is interrupted by multiple unconformities as well as sections of tephra and gravels. Characterization of the laminations and banding throughout the 10 meters of core, including characterization of fine (~1mm) laminations in a 1 meter section, and understanding their link to the regional environment, will aid in reconstructing the history of sediment deposition at this location in response to sub-millennial timescale environmental change. XRF profiles of elemental concentrations across the laminated core section reveal quasi-cyclic variability in multiple environmental variables that represent various aspects of the lake catchment system and at several frequencies. For example, high Si:K and Ca content are interpreted to represent increased diatom productivity and autochthonous carbonate precipitation in the lake, respectively, and vice versa. Microfacies analyses of thin sections and sediment slabs provide a qualitative assessment of dark and light laminae and aid in assessing the relationship between elemental content, minerals, and lacustrine processes. Spectral wavelet analyses were conducted on data from the finely laminated Olorgesailie sediment core and on both the modern and Last Glacial Maximum sedimentary deposits from Lake Challa (Wolff 2011), which is located 240 km from the Olorgesailie paleolake and serves as a modern analogue for comparison. Through this comparative analysis, we interpret the paleoenvironmental results from the Olorgesailie sequence in the context of the Pleistocene epoch.

TABLE OF CONTENTS

LIST OF TABLES

LIST OF FIGURES

1. Introduction

1.1. Hominin Evolution in the East African Rift

Paleoclimate records reconstructed from ocean and ice cores provide a broad outline of global changes in climate over millions of years. While exceptionally valuable in developing our understanding of how the planet responds to changes in orbital forcing, these records do not provide the spatial information and, in some cases, temporal resolution needed for understanding climate change on scales that are relevant to mammalian evolution. Proxies derived from lake sediments give insight on the climate at local to regional scales that global climate proxies cannot provide. Lakes have a higher sedimentation rate than the ocean, so they record environmental change with resolutions that are more directly relevant to evolutionary processes. However, lake sediments are much more variable, responding to regional climate, tectonics, and lithology of the catchment. Although these complications result in challenges in interpreting climate signals in lake sediments, they also provide local, basin scale information that is invaluable for developing the low latitude, terrestrial perspective on paleoenvironmental change that is essential for understanding the evolution of hominins.

Interest in the linkages between human evolution and the Earth's climate has grown in recent years as ongoing climate change has become more evident. The East Africa Rift System (EARS) has long been hailed as the setting of hominin evolution through the Pliocene and Pleistocene (Potts et al. 1994); yet we have lacked critical information on changes in the climate of this region.

Understanding regional and local paleoclimate in the context of the better established global climate history requires local high-resolution records. East Africa experienced major wet periods characterized by lake expansion and development during the Late Cenozoic (Trauth et al. 2005), and the sediment sequences of these lakes have the potential to contain such records. Within the southern Kenyan Rift valley, the Olorgesailie basin is known for a dense distribution of hominin artifacts from the Pliocene and Pleistocene. Many of these artifacts are tools, such as hand-axes and Acheulean bifaces (Potts et al. 1999). The Olorgesailie formation is divided into 14 members consisting of diatomaceous, tuff, and gravel beds that span 0.5-1Ma, providing a wide but discontinuous record of sedimentation in the basin (Deino & Potts 1990). Using sediment cores from the Olorgesailie paleolake, we can reconstruct the mid-Pleistocene paleoclimate and paleolandscape in which these hominins lived.

1.2. Tectonic and Volcanic History of the EARS

In order to reconstruct the paleoclimate of the EARS, effects of different forcings on the climate must be examined. On millennial time scales, regional climate in East Africa is controlled by tectonic forcing (Trauth et al. 2007). Regions with high relief have more complex climate systems and experience local climate changes that are not simply responses to global climate forcing (Trauth et al. 2005). Progressive uplift and rifting has caused East Africa to dry over the Cenozoic, but the northern and the southern portions of the EARS are climatically distinct (Maslin et al. 2007). Several small lakes occupied the basins in the East/North branch of the Rift Valley during the Plio-Pleistocene (Trauth et al. 2007). These paleolakes formed earlier, and were much smaller, than their southwestern counterparts (Trauth et al. 2007). This broad trend is true today;

the northern portion of the EARS is arid while the southern portion currently holds some of the World's largest lakes.

Along with tectonic activity during the Cenozoic in East Africa, there is also an extensive history of volcanic activity in Ethiopia, Kenya, and Tanzania. Both tectonic and volcanic activities have influenced sedimentation in the rift valley (Trauth et al. 2007) (Figure 1.2.1). Magmatic activity in the central and southern parts of the rift, where Olorgesailie is located, began between 16 and 8 million years ago (Ma) (Ebinger et al. 2000, Trauth et al. 2005). Major faulting occurred in the Magadi-Natron-Olorgesailie basins 1.2 Ma, resulting in the rift escarpments present today (Foster et al. 1997). In the Olorgesailie Formation outcrops, there are layers of alternating lacustrine and subaerial sediment that date between 0.922 and 0.452 Ma (Trauth et al. 2005).

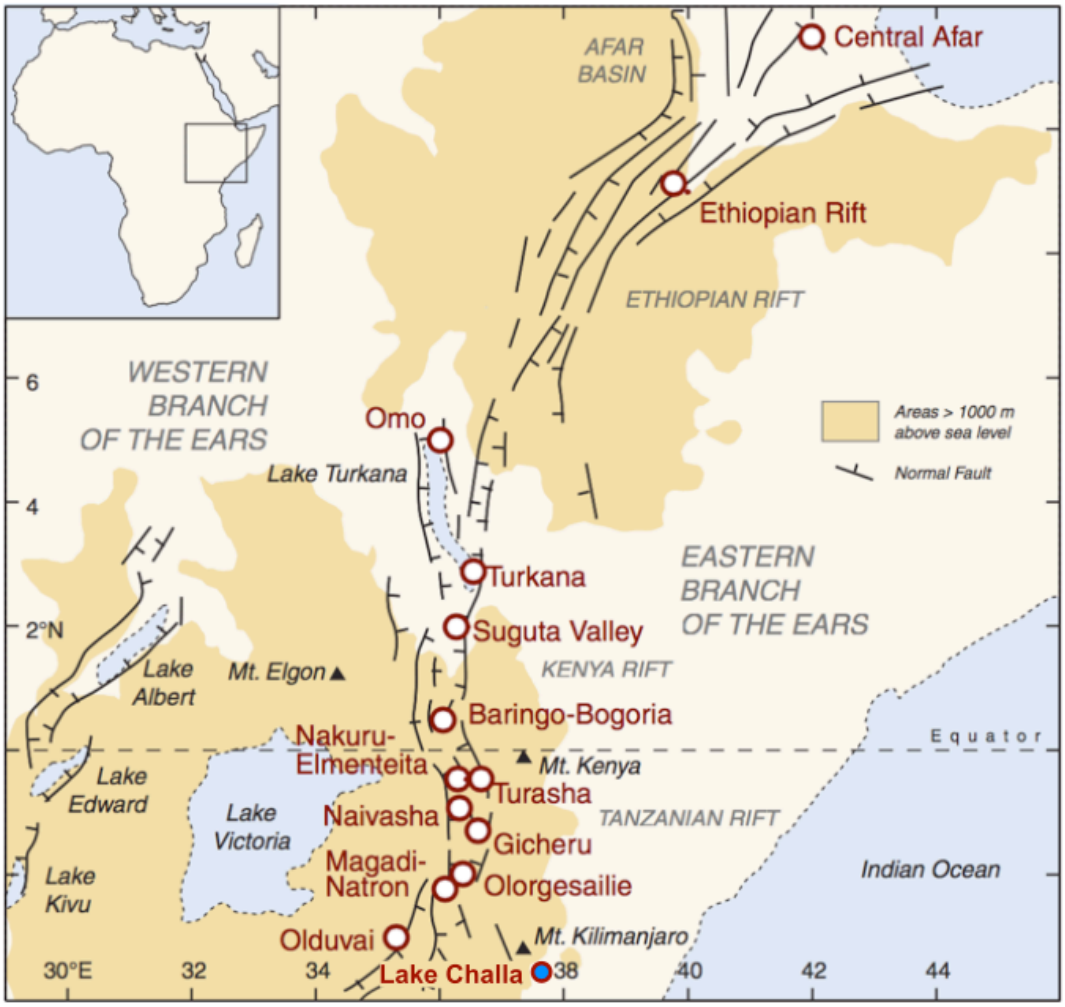

Figure 1.2.1: Map of EARS

Map of East Africa, showing faults in the northern section of the EARS and selected basins (Trauth et al. 2005)

The volcanic and tectonic setting of this region created the rift basins, which were or currently are occupied by lakes. In order for lakes to exist, the climate must, at least annually, provide a positive moisture balance. There are different scales and responses times of climate forcing that could have contributed to a positive moisture balance in East Africa during the late Cenozoic. and that are important for understanding the driving factors of past sedimentological and climate change signals in the lake records. Of great importance, the amount of solar insolation at a given point in time is key to

reconstructing the paleoclimate. Insolation can be calculated by combining the effects of eccentricity, obliquity, and precession on changes in Earth's orbit (Milankovitch 1949). The magnitude of the effect on climate caused by changes in insolation varies depending on the latitude (Maslin et al. 2001). Although, the impact of orbital forcing on high latitude climates and late Cenozoic global climate transitions is well studied (Maslin et al. 2007), there is still much that is not understood about the effect of orbital forcing on the tropics.

1.3. Paleoclimate Records in EARS

Records of moisture availability in the tropics during the Pliocene and Pleistocene (deMenocal, 1995, 2004), along with climate modeling experiments (Clement et al. 2004), show that precessional forcing could have as strong an effect on seasonality as glacial-interglacial cycles (Maslin et al. 2007). Strong evidence of cyclical millennial climatic change in many formations in the EARS, including the Olorgesailie Formation, has been linked to orbital forcing (Maslin et al. 2007, Trauth et al. 2007). Other late Cenozoic climate transitions observed in other regions must be considered in the EARS (Maslin et al. 2007). Evidence of mega-droughts has been seen during the Pleistocene in cores from Lake Malawi, in the southern part of the EARS (Cohen et al. 2007). Another example is the development of the Walker Circulation, which marks the beginning of the strong easterly trade winds that maintain the east west gradient of sea surface temperatures in the Pacific Ocean (Maslin et al. 2007). This started at 1.9Ma and coincided with pluvial episodes of lake expansion in some locations within the northern EARS (Trauth et al 2007). The Walker Circulation is a critical atmospheric component of the El Nino-Southern Oscillation (ENSO), which has a

strong influence on drought/pluvial cycles in some areas of Africa (Maslin et al. 2007).

The Hominin Sites and Paleolakes Drilling Project (HSPDP) along with the Smithsonian's Human Origins Program team drilled cores from six different paleolake sites, including Olorgesailie, within the northern part of the EARS from 2012 to 2014. The Olorgesailie basin, which is home to some of the richest evidence of Cenozoic hominin tool making, contains a sediment record of the paleolake that once occupied the basin (Potts 1999). The cores have many sections of tephra events, gravel, turbidites, and paleosols that punctuate the record and complicate the age model. Amidst the diversity of sediment within the core, there are a few laminated sections, indicative of a deep lake. Although discontinuous, the Olorgesailie basin sediment record provides insight into the paleolandscape and climate of a region that contains an abundance of hominin artifacts and thus evidence for long periods of hominin occupation.

1.4. Research Aims

Three main research questions will be explored in this thesis. What depositional environments were present in the Olorgesailie basin during the time interval that these lacustrine sediments were deposited? Are the couplets in the finely laminated section varves? What does this mean in the context of paleoclimate change in the greater East African Rift Basin?

Chapter 3 focuses on the elemental and microfacies variations within the 10 lacustrine core sections, using multiple types of imagery, XRF proxies, and a PCA ($PCA_{10\text{-}sec}$). Results from three of the ten core sections are compared in order to infer distinguishing characteristics of their depositional environments. In Chapter 4, core section ODP-OLO12-1A-63Q-2 is examined in greater detail

including a principal component analysis (PCA) of the finely laminated section alone ($PCA_{1\text{-}sec}$). The working hypothesis that the fine laminations are varves is tested through wavelet analyses of $PC1_{1\text{-}sec}$ and comparison between the core section's varve thicknesses to wavelet analyses of Lake Challa's modern sediment and varved sediment from the last glacial maximum (LGM) (Wolff 2011). Lake Challa's coupleted sediments (both modern and LGM) have been analyzed and compared with seasonally monitored sediment traps, and thereby have been conclusively shown to be varves that record cyclical climate signals (Wolff 2011). The hypothesis that the finely laminated section is varved will be supported if the periodicities identified via wavelet analyses of the Olorgesailie sequence are similar to the periodicities determined via spectral analysis of the Lake Challa sediment record. This multifaceted investigation will help to place the findings from the Olorgesailie lacustrine sequence in the greater Pleistocene paleoclimate context.

2. Materials & Methods

2.1. Previous analyses on the sedimentary sequence of the OLO basin

Drill cores from two sites (Figure 2.1.1) in the Olorgesailie Basin were collected in 2012 as part of The Smithsonian's Human Origin Program. The Olorgesailie cores have been subject to initial analyses, including initial X-ray Fluorescence (XRF) core scanning, optical and x-ray imagery, grain size distribution, diatom and ostracod classification, authigenic mineralogy classification, and carbon and oxygen isotopic ratios (unpublished workshop materials, 2014). Most of the lacustrine sequence is characterized by banded or massive silts and clays. There is a unique section between 105 and 135 meters below surface (mbs) that is laminated in a manner similar to modern varved sequences and appears to be evidence of a deep lake (unpublished workshop materials, 2014). Elemental and microfacies characterization of the ~1mm laminations in this 30-meter section could be a key to linking past regional environmental changes to sediment deposition in this location. Understanding the processes of sediment formation and depositional environment of the Olorgesailie basin will lead to a stronger paleoclimate reconstruction of this critical site of early hominin tool use technology.

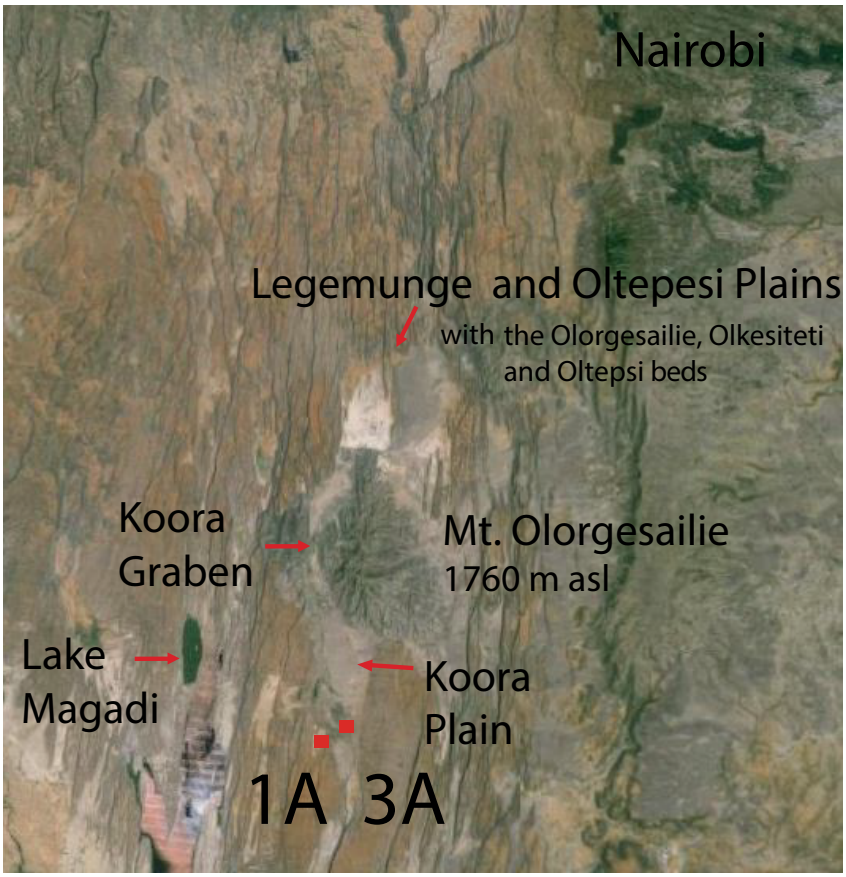

Figure 2.1.1: Map of Olorgesailie Drill Sites
Drill sites 1A and 3A marked on map of Olorgesailie basin (Stockhecke unpublished)

2.2. Elemental analysis of sediment cores using the Itrax XRF Core Scanner

The main instrument used in this thesis was the Itrax X-Ray Fluorescence Core Scanner at the Large Lakes Observatory (University of Minnesota), which performs non-destructive, continuous X-Ray Fluorescence (XRF) analysis while also taking x-radiographic and photographic imagery. The X-Ray imagery displays changes in density through the core, showing laminations or evidence of bioturbation that may not be discernible on the core surface. The XRF elemental data can be used in ratios as proxies for different environmental conditions. The

raw counts of each element of the XRF scanning are normalized with standard reference materials.

The initial core description and imagery from the Olorgesailie cores show a number of sections within the cores that are finely laminated, indicating lacustrine deposition (unpublished workshop materials, 2014). After using the Corelyzer software (full core imagery) followed by physical inspection of some cores, ten laminated sections were selected for further analyses (core imagines in Appendix). These ten sections were scanned with the Itrax XRF core scanner under 60kV and 50mA, for 200 msecs every 0.2mm to create high-resolution profiles of elemental concentrations through the lacustrine sections. To avoid scanning cracked sections, the core sections were offset laterally within the Itrax XRF chamber. The sediment cores were run with a molybdenum source tube over the course of six weeks.

The high-resolution XRF allows us to identify changes in the elemental concentrations within individual laminations. Fluctuations in elemental concentrations and ratios are used as proxies for a range of paleoenvironmental conditions. For example, Si:Ti has been used as an indicator of biogenic silica, which can indicate high levels of productivity. In the EARS, the Rb:K ratio has been used a proxy of the extent of weathering of the soil in the catchment, as K is more preferentially removed over Rb during chemical weathering of mica and feldspars (Brown et al. 2011). Some elemental concentrations are used as proxies on their own. For example, high Ca concentrations indicate preservation of calcite in the sediments, an indicator of arid conditions (Brown et al. 2011). Ti content has been used globally as an indicator of clay content, as titanium is an immobile element found in clays, and often represents rates of catchment erosion (Katsuta et. Al. 2007, Brown et al. 2007, 2011). We will apply proxies to the XRF data from Olorgesailie that have been used in the region before, such as Rb:K, Si:Ti, and Ca (Brown et al. 2007, 2011, Johnson et al. 2011).

2.3. Radiometric dating, floating varve chronology, and sedimentation rates

The finely laminated core section was selected for lamination counting and age model analysis, as the bands in the other sections are too thick to likely be annual deposits. The finely laminated section could be varved (annual laminations), a hypothesis which is investigated in the Fine Laminations chapter.

Laminations in the finely laminated section (ODP-OLO12-1A-63Q-2) were counted using two different methods: manual counting on a color composite image and an Excel macro on a grey scale composite image. The couplets were manually counted five separate times using the whole core images, resulting in an average count of 834 couplets (+/- 20). There are two tephra layers in this core, visible from both from XRF data and visual assessment. These tephras were assumed to be instantaneous events, and their thicknesses were removed from the overall length of the section. The manual sedimentation rate was calculated by dividing the total number of laminations by the length of the section (minus the tephra layers). The sedimentation rate of the manual counting was 1.24 mm/yr.

A composite grey scale image of the finely laminated section (OLO-ODP12-2A-63Q-2) was analyzed with varve counting Excel macros (Figure 2.3.1). The Layer Recognition (BMPix) and Counting (PEAK) Excel macros determined the depth of each couplet and assigned depths in accordance with those thicknesses (Weber 2012). This software counted 767 couplets, with 220 deemed “too narrow” to count. This lamination data set was used as the working age model for the Principle Component Analysis ($PCA_{1\text{-}sec}$) and spectral wavelet analysis. This software also calculated an sedimentation rate, which varies with

depth, but averages 1.38 mm/yr (Figure 2.3.3). This software also extracted varve thickness data, which was analyzed via spectral wavelet analysis.

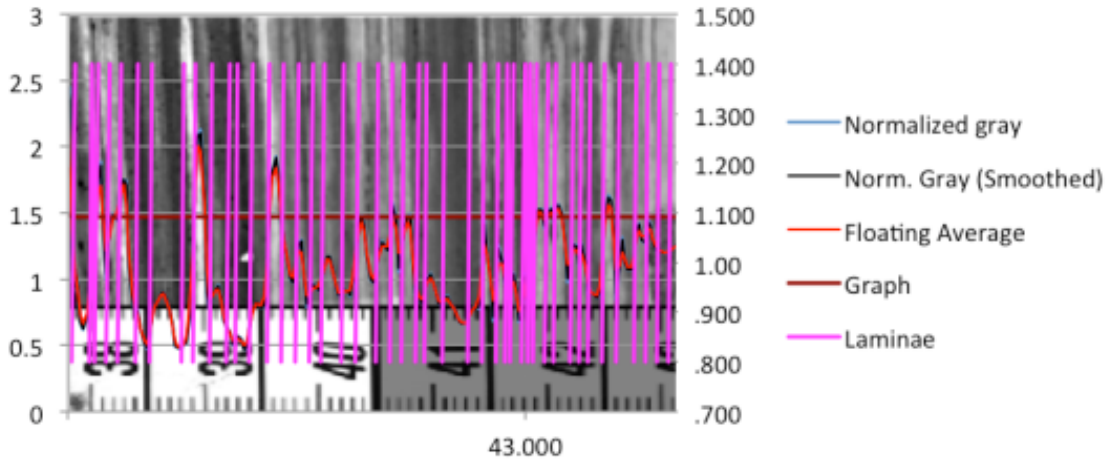

Figure 2.3.1: BMPix and PEAK Varves
Sample of the figure produced by the varve counting software using grey scale composite image. Pink lines mark boundary between couplets

Preliminary Ar/Ar dates have been assigned throughout the core (Deino personal communication, 2016), three of which were used to estimate a third sedimentation rate (Figure 2.3.3). The sedimentation rates vary between the three different methods; however the manual counting and the automatic counting sedimentation rates are more similar to each other and both an order of magnitude larger than the Ar/Ar date sedimentation rate (Figure 2.3.3). Throughout the suite of cores, there are many erosional discontinuities that could provide an explanation for the order of magnitude difference between the sedimentation rates calculated from varve counting (both manual and automatic) and the Ar/Ar sedimentation rate.

The age of the three subsampled sections were estimated with the best-fit line between the three Ar/Ar dates (Figure 2.3.2). The deepest core section, OLO-ODP12-71Q-2 at 133.07 - 134.64 mbs, lies outside of the Ar/Ar date range. The approximate age for this core section was estimated by extrapolating the linear best-fit line through the three dates (Figure 2.3.2).

Depth (mbs)	104.6	120.9	131.9
Ar/Ar Age (ka)	251	335	400

Table 2.3.1: Preliminary Ar/Ar ages near studied interval
Three preliminary Ar/Ar ages at depths near three subsampled core sections. Uncertainty range on Ar/Ar dates is +/-5 ka

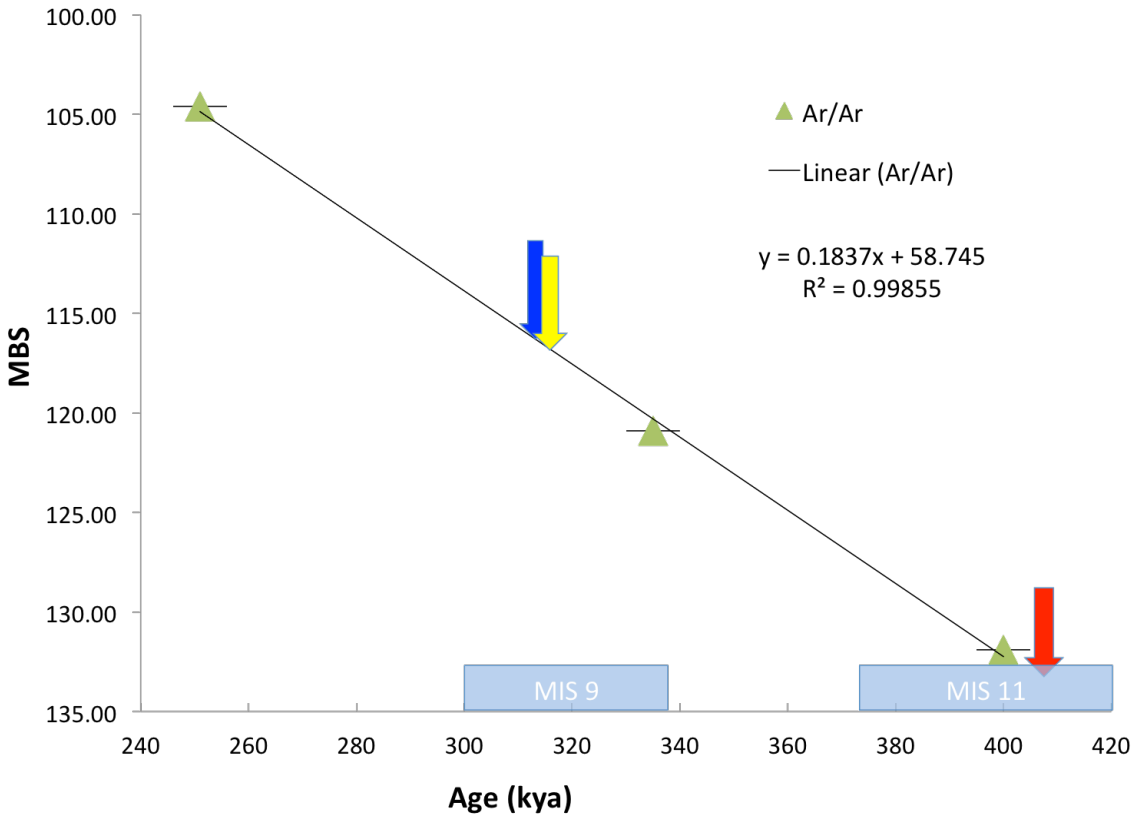

Figure 2.3.2: Ar/Ar age model with floating varve chronologies
Three Ar/Ar dates plotted with best-fit line. Depth of three subsampled core sections marked on best-fit line. Blue arrow marking section 63Q-1, yellow arrow marking section 63Q-2, and red arrow marking section 71Q-2.

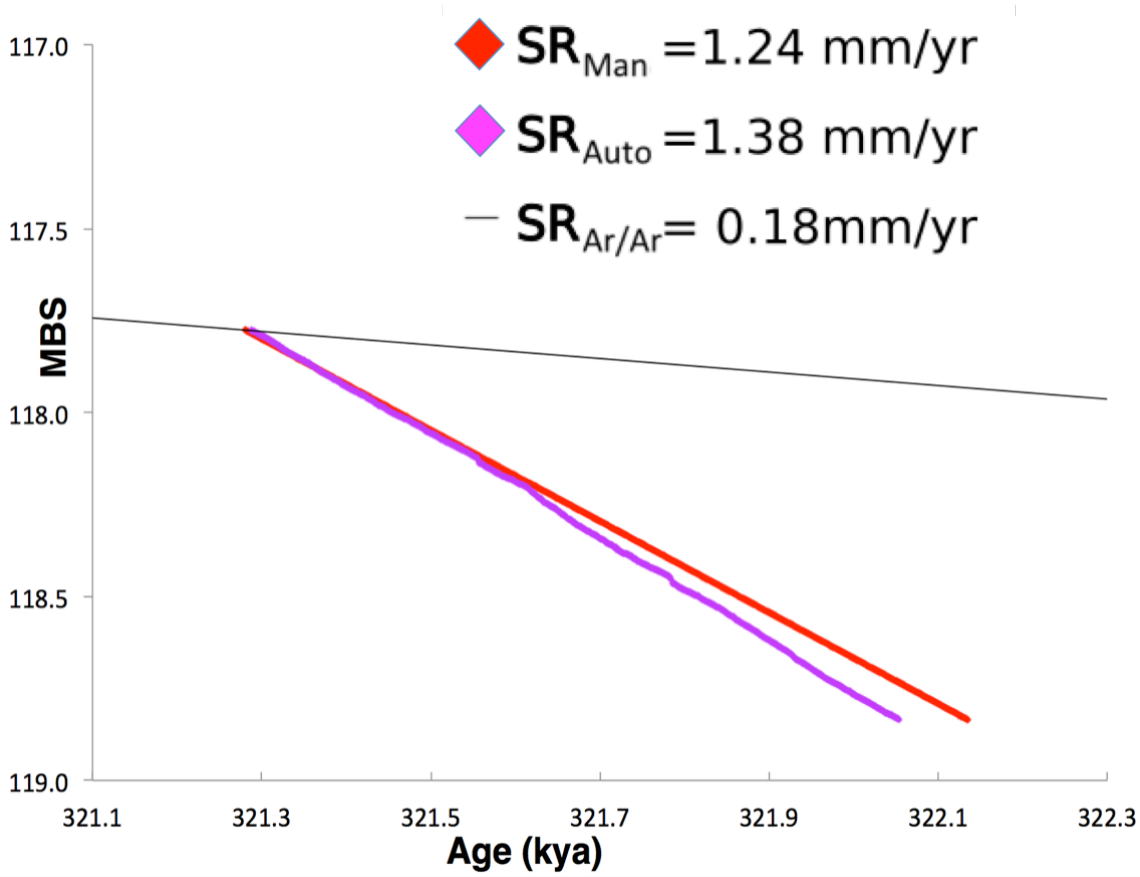

Figure 2.3.3: Floating varve chronologies and sedimentation rates
Floating varve chronologies (from manual and automatic varve counting) anchored to Ar/Ar best-fit line, corresponding with depth at top of core section ODP-OLO12-63Q-2. Sedimentation rates of Ar/Ar age model, manual counting varve chronology, and automatic varve chronology noted.

2.4. Microfacies analysis on embedded sediment slabs and thin sections

Three of the ten cores were identified as displaying distinctly different laminations or banding (OLO-ODP12-63Q-1 116.41-117.74 mbs, OLO-ODP12-63Q-2 117.77 - 118.83 mbs, and OLO-ODP12-71Q-2 133.07 - 134.64 mbs) and were chosen to be subsampled for microfacies analysis. Subsampling was completed at LacCore (University of Minnesota). Four subsamples were collected

and impregnated with epoxy (5 to 10cm, see Appendix), two from core section 63Q-2. From each embedded sediment slab, thin sections and polished epoxy-blocks were produced. Thin sections were analyzed with a light microscope and a photographic scanning light microscope to characterize the microfacies and to select areas for SEM/EDS analysis.

The epoxy-blocks were used for scanning electron microscope (SEM) and energy-dispersive x-ray spectroscopy (EDS, University of Minnesota Duluth). SEM backscatter images were taken to characterize microfacies and point EDS analysis made to identify chemical content of single grains within the sediment matrix. The mineralogical and chemical data from the SEM/EDS was subsequently compared with the high-resolution elemental concentrations to determine their relationship.

2.5. Counting the light/dark couplets of the finely laminated section

The layered sediments of the three selected core sections were evaluated using microscopic imagery and whole core images. Thin sections were photographed using LacCore's Leica DMLP microscope with a Leica DFC420 camera. The images were stitched together by the accompanying software, Leica Applications Suite v.4.6.0. These images were used to confirm lamination terminations based color and lithological makeup (clay grains, diatoms, etc.). Laminations were also counted using the whole core images. After calculating rough sedimentation rates based on lamination counting, only the finely laminated section (OLO-ODP12-2A-63Q-2) was selected for further age model analysis. A composite gray scale image of the finely laminated section was used to count laminations using the Layer Recognition (BMPix) and Counting (PEAK)

software**.** The automatic varve counting software measured the thickness of each couplet and assigned depths in accordance with those thicknesses (Weber 2012).

2.6. Statistical data analyses

Principal component analyses (PCA) were performed on the entire ten-core section dataset ($PCA_{10\text{-}sec}$) and on one section (ODP-OLO12-1A-63Q-2) with the most distinct laminations ($PCA_{1\text{-}sec}$). The PCA was conducted by following “A tutorial on Principal Component Analysis” (Smith 2002) and the MATlab function “coeff().”. The nine elements assessed with the PCA were Si, Ti, K, Ca, Mn, Fe, Rb, Sr, and Zr. These elements were chosen because of their known application as paleoclimate proxies (see section 2.2)**.** Element counts were standardized using zscores before the PCA was conducted. The first PCA was applied to the ten cores section ($PCA_{10\text{-}sec,}$ 442,098 data points) and the second PCA was applied to the finely laminated section only ($PCA_{1\text{-}sec,}$ 47,700 data points)

Additionally, spectral wavelet analysis was performed on the finely laminated section $PC1_{1\text{-}sec}$ data and varve thickness data (OLO varve thickness) using floating varve chronology from the automatic varve counting software (Torrence and Compo 1998). Published spectral wavelet analysis performed on the Challa modern and LGM varve thickness data (Wolff 2011) was compared with the OLO varve thickness. The spectral wavelet analyses are discussed in chapters 4.3 and 4.4.

3. Microfacies Analysis

3.1. Sedimentological Characteristics

Three sections (OLO-ODP12-1A-62Q-3, OLO-ODP12-1A-63Q-2, and OLO-ODP12-1A-71Q-2) best exemplified the three lithologies observed in the interval covered by the ten analyzed sections of the Olorgesailie lacustrine clays (Figure 3.1.1).

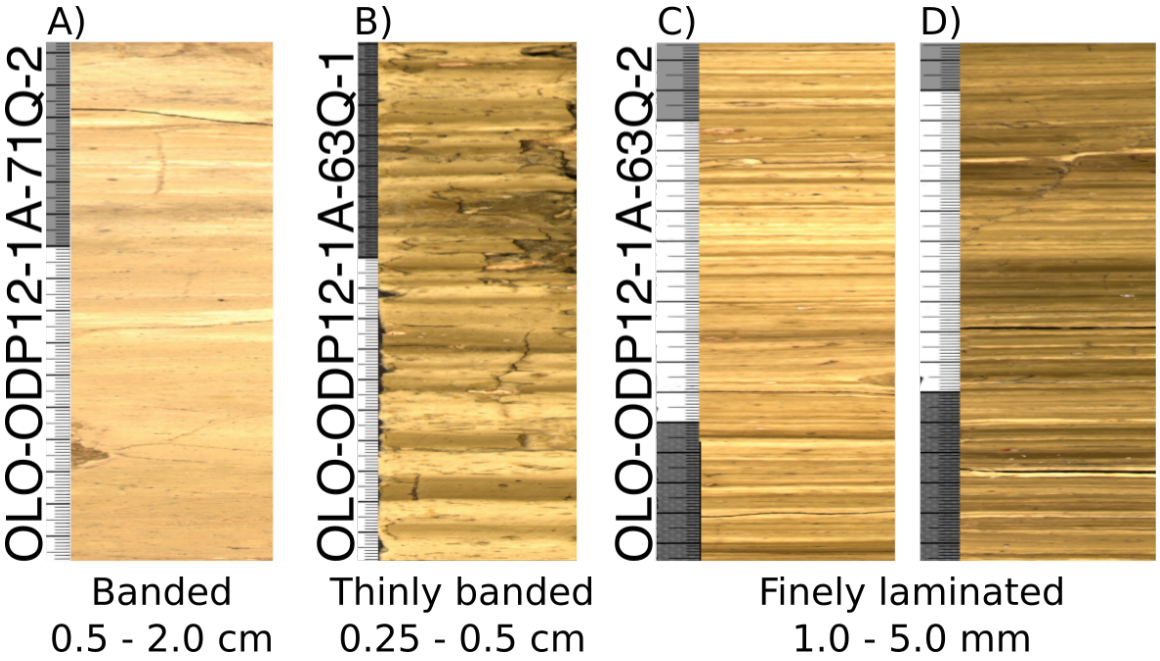

Figure 3.1.1: Core sections showing three types of banding/lamination

Section 71Q-2 (Figure 3.1.1 A) is composed of alternating bands of beige and lighter beige color, ranging in thickness from 0.5 – 2 cm. There are parts of this core section that do not have alternating bands, and are visually homogenous in color (Figure 3.1.1 A). The bands fade into one another and do not have clear boundaries. This section will be referred to as the banded section.

Throughout this core section, the bands range in thickness. In some parts there are alternating couplets (as shown in Figure 3.1.2), while other parts of the core are either just the lighter or darker color. Calcite crystals were identified both under optical microscope analysis and SEM imagery (Figure 3.1.2). The lighter bands mainly consist of massive calcite. The darker layers are also calcareous but they contain calcite grains interspersed with clay and broken diatom frustules. The diatoms in this section are much less abundant than in the thinly banded and finely laminated sections, and they are poorly preserved where present (pieces rather than whole frustules). In the banded section, both light and dark colored bands contain higher levels of calcium than any of the sediments of the other two sections. While the light and dark alternating bands are visible in the optical images, the boundaries between the bands are gradational under light microscope analysis.

Sediment in section 63Q-1 (Figure 3.1.1 B) has couplets ranging in size from 0.25 – 0.5cm. These couplets have a greater color contrast than the layering of the banded section, alternating between yellowish beige to light brown (Figure 3.1.1 B). Boundaries between these thinner bands are generally distinct, but there are some sections of the core in which the bands fade gradually within and between couplets. While the couplets range in size, most are thinner than the layers of the banded section. This section will be referred to as the thinly banded section.

The thinly banded section contains light and dark bands that are mostly present in couplets. Optical microscope examination revealed that the darker bands are clay rich, with a few interspersed calcite grains and diatoms (Figure 3.1.3). There are few ostracod shells preserved in these sediments, as seen in the top of the middle optical microscope image in Figure 3.1.3. Light bands are mainly made up of diatoms, which are very well preserved. Dark bands are predominantly clay rich with some interspersed calcite grains and diatoms. Boundaries between the bands range from very sharp (as seen in the middle SEM image in Figure 3.1.3) to slightly gradational (B, Figure 3.1.1).

Section 63Q-2 (Figure 3.1.1 C,D) has the finest laminations of the 10 sections. These laminations are distinct couplets ranging in color from yellowish beige to light brown couplets (Figure 3.1.1 C) or light brown and dark brown couplets (Figure 3.1.1 D), with thicknesses from 1mm to 5mm. Visual inspection indicates the boundaries between the fine laminations are sharp. This section will be referred to as the finely laminated section.

In the finely laminated section, light and dark layers are consistently found in couplets that have a thickness of 1.0 to 5.0mm. The couplets range in color, but always contain a light and dark lamination, as seen in the difference between D and C in Figure 3.1.1. Optical microscope analysis revealed that both light and dark laminations contain well-preserved diatoms (Figure 3.1.4). The light laminations are mainly made up of diatoms with some calcite grains. The dark layers are predominantly clays with some interspersed diatoms. The terminations between these laminations are very distinct (middle, Figure 3.1.4).

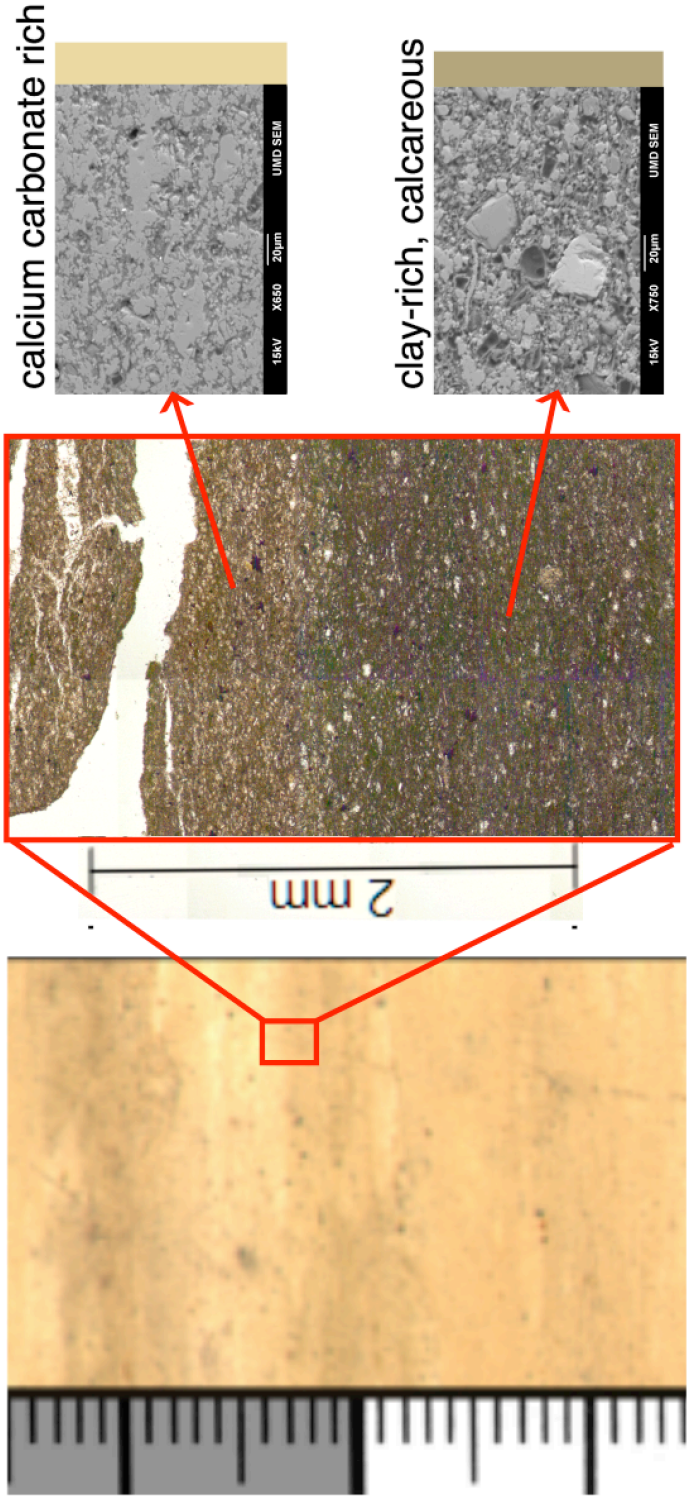

Figure 3.1.2: Optical microscope and SEM imagery of bands.

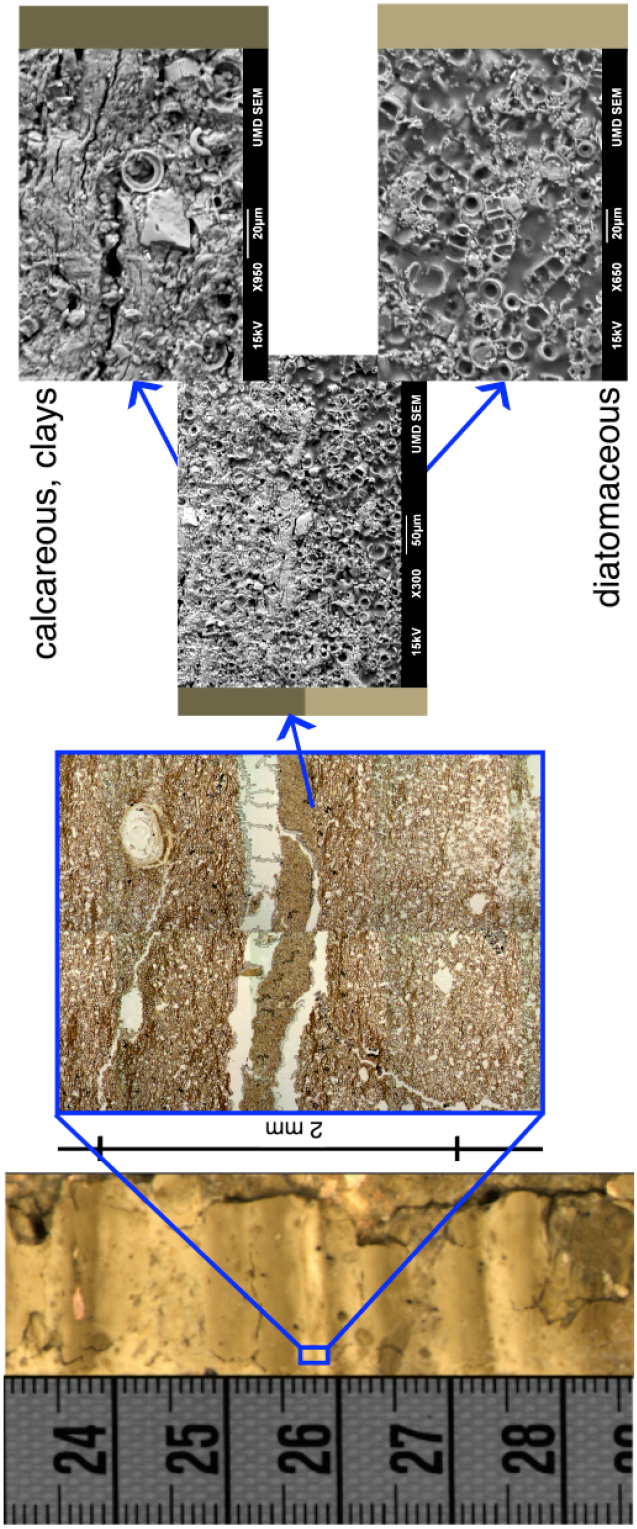

Figure 3.1.3: Optical microscope and SEM imagery of thin bands.

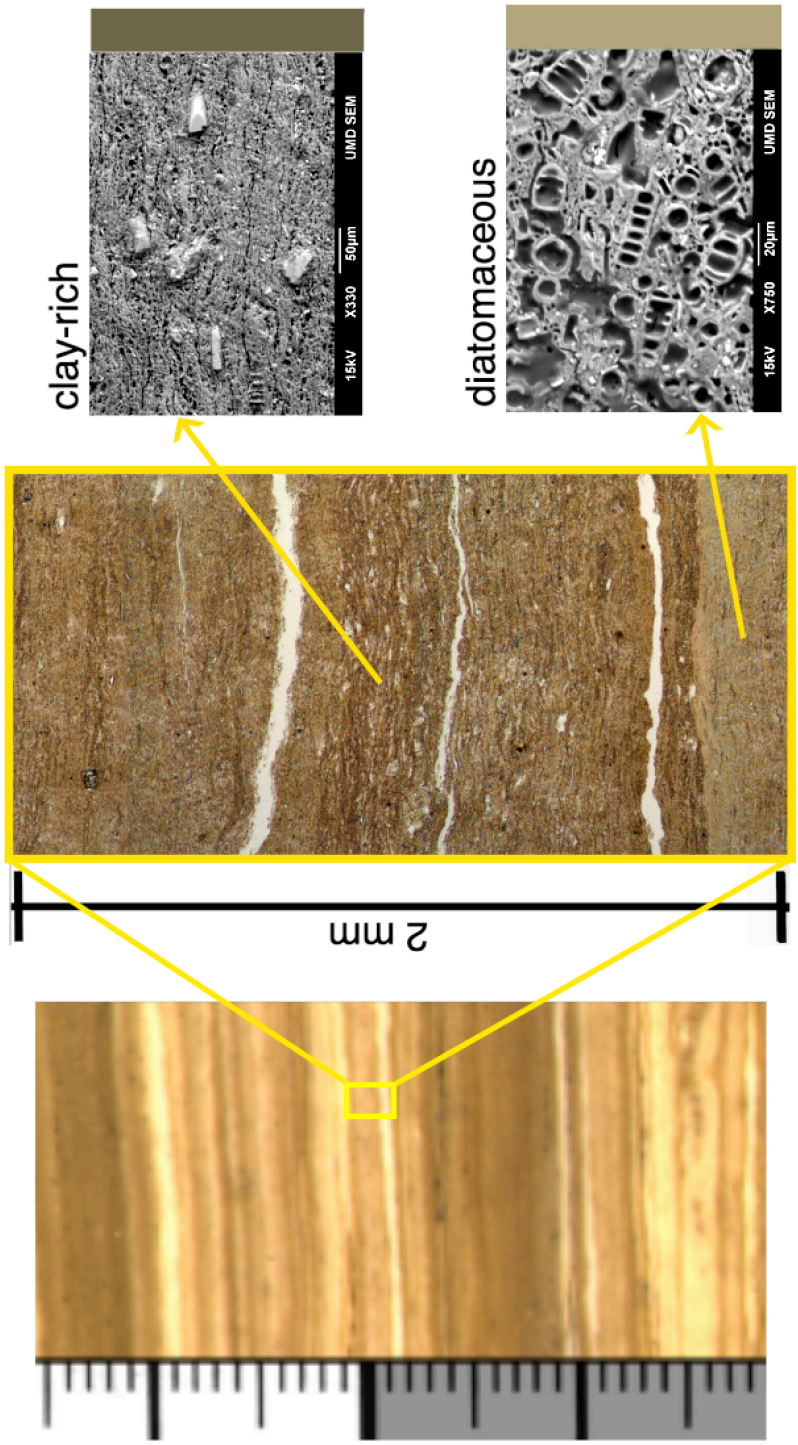

Figure 3.1.4: Optical microscope and SEM imagery of fine laminations.

3.2. Elemental variability

While these three sections have distinctly different physical characteristics, apparent in the optical, x-radiographic, and microscopic images, the XRF data reveals both similarities and further differences in their chemical distribution and composition. Scans of the cores at 0.2mm resolution reveal elemental differences within the couplets. In order to assess the elemental makeup of the cores, selected element percentages and ratios were superimposed on the core image for visual verification of correlations. The main proxies used were Si:Ti as the biogenic silica proxy, %Ti as the proxy for clays, and %Ca for calcium carbonate. %Ti alone has been used as an indicator of clay concentration in the EARS and in other regions, as titanium is abundant in clay minerals (Katsuta et al. 2007, Brown et al. 2007, 2011). Si:Ti has been used as an indicator of biogenic silica from diatoms, having a positive correlation with lake productivity (Brown et al. 2007, 2011, Johnson et al. 2011). High Ca concentrations indicate preservation of carbonate minerals (e.g., calcite) in the sediments, which often occurs under arid conditions (Brown et al. 2011).

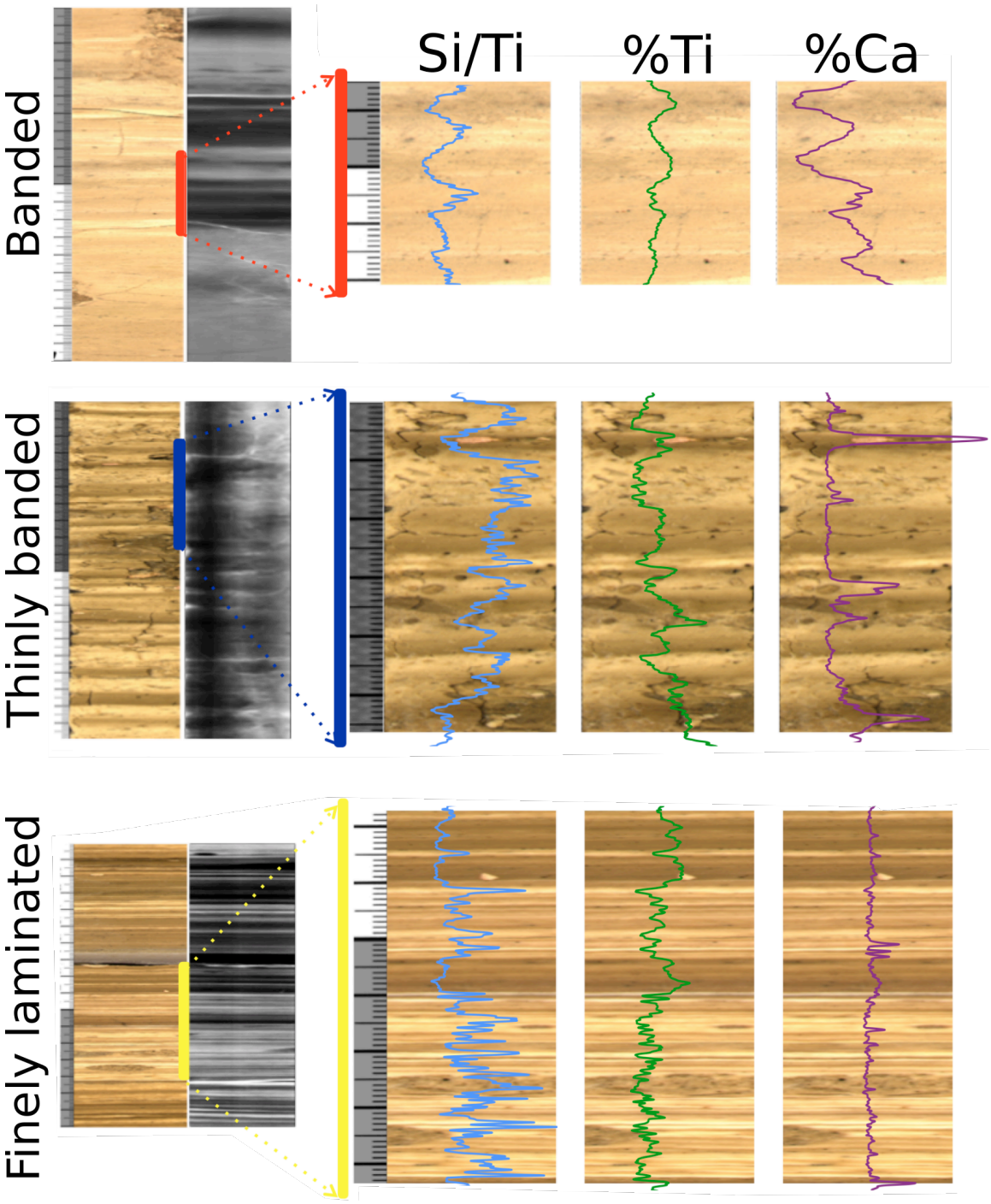

Figure 3.2.1: Interpretations of XRF scan data.

In all three sections, the biogenic silica proxy is associated with lighter layers, and the clay proxy is highest in the darker layers. Differences between the three lithologies are apparent in the strong variability of the calcium content (Figure 3.2.1). The banded sediments contain high levels of calcium (corresponding to ~15 to ~60% $CaCO_3$ assuming Ca is bound in Calcite only). The bands are comprised of carbonate rich layers containing some diatomaceous layers that alternate with clay-rich calcareous layers.

Within the thinly banded section, some bands have relatively high Ca ($CaCO_3$ up to ~15%), which is mostly due to concretions within the sediment. The light bands are biogenic silica-rich and the dark bands are clay-rich. The lighter bands also contain higher amounts of biogenic silica than their darker counterparts.

In the finely laminated section, the light laminations are abundant in biogenic silica and the dark laminations are predominantly clays. Calcium carbonate is present at some intervals, but generally has very low abundances throughout this section, with sharp peaks associated with concretions in the thinly banded and the finely laminated sections.

3.3. Principal Component Analysis (PCA) on 10 core sections

A Principal Component Analysis ($PCA_{10\text{-}sec}$) was conducted on the high-resolution XRF data from the 10 lacustrine sections. Of the 35 elements in the XRF output, only 9 were included in the $PCA_{10\text{-}sec}$. Si, Ca, and Sr were chosen as tracers for diatoms, ostracods, and calcium carbonate, respectively. Ti, K, and Mn were chosen as indicators for clay content. Zr and Rb are indicators of weathering of volcanogenic soils from the Olorgesailie catchment. Lastly, Fe and

Mn were chosen as indicators of iron and manganese oxides formed by diagenetic or pedogenetic processes. The analytical concentrations of individual elements and their variability through the cores sections varies greatly among these nine elements, so their counts were normalized with z-scores in order to equalize their variance prior to PCA.

Principal Component	PC1	PC2	PC3	PC4	PC5	PC6	PC7	PC8	PC9
Eigen Values	0.37	0.26	0.12	0.10	0.05	0.04	0.03	0.02	0.01

Table 3.3.1: Eigenvalues of each Principal component

Normalized eigenvalues of each $PCA_{10\text{-sec}}$ indicate the amount of the overall variance in the data set that the PC represents. The first PC, or $PC1_{10\text{-sec}}$, represents 37% of the variance within the data (Table) and has very positive loadings with elements reflecting clay content and a negative loading with calcium. We therefore assert that PC1 captures the fluctuations in clay content throughout the core sections.

The second principle component, $PC2_{10\text{-sec,}}$ contributes 26% of the variance in the data (Table 3.3.1), and has positive loadings with carbonate forming elements: calcium, manganese, and strontium (Figure 3.3.1). $PC2_{10\text{-sec}}$ characterizes the fluctuations in calcium carbonate throughout the dataset.

The third and fourth principle components represent far less variance than do the first two, only 12% and 10% respectively (3.3.1). $PC3_{10\text{-sec}}$ strongly loads positively with iron and slightly negatively with the clay elements, reflecting iron oxides in the sediment (Figure 3.3.1). $PC4_{10\text{-sec}}$ loads very strongly with silica, and reflects the variation in biogenic silica (diatoms) in the cores (Figure 3.3.1).

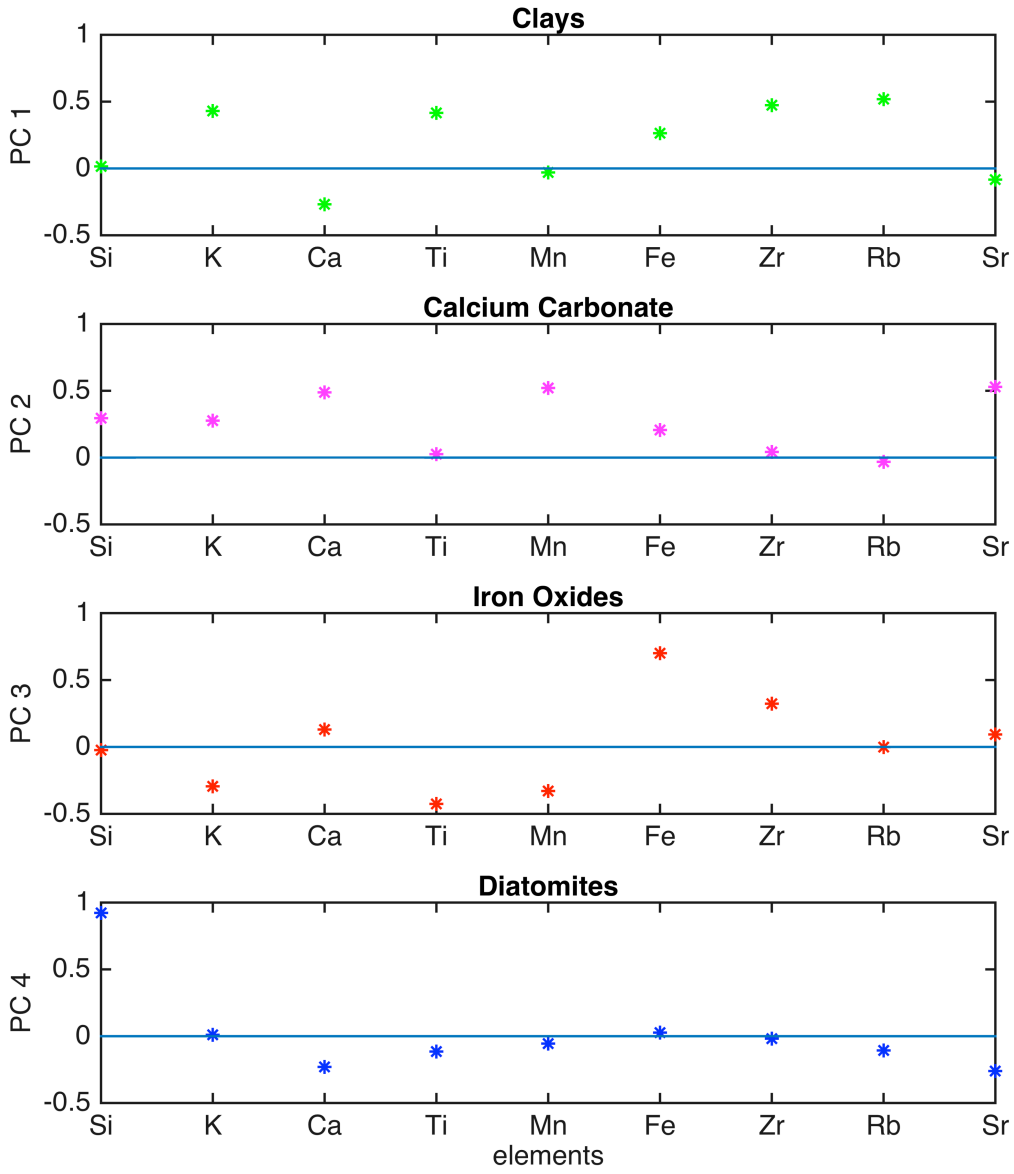

Figure 3.3.1: Element loadings of the first four Principal components.

The PCA quantifies variance over the 10-core suite, which contains a diverse array of lacustrine sediment types. Therefore it is not surprising that the $PCA_{10\text{-}sec}$ does not capture small variations within individual sections as well as it distinguishes different sections from each other. On the scale of laminations, the elemental data more closely follows changes within the sediment much more

accurately than the $PCA_{10\text{-}sec}$ (Figure 3.3.2). For example, while the clay component, $PC1_{10\text{-}sec}$, shows broader changes on the scale of 2 to 5mm that follow clay content (also visible as darker color in the sediment), it does not capture the inter-lamination changes that are clearly reflected by changes in elemental concentrations (Figure 3.3.2).

$PCA_{10\text{-}sec}$ reveals broad changes between the core sections that distinguish them from each other. Although the ten sections of core are from the same lake system and span a relatively short depositional interval (about a 30m range), they are nevertheless punctuated with tephras, paleosols, and erosional discontinuities. $PCA_{10\text{-}sec}$ demonstrates how the sections vary from each other on a 10cm - 100cm scale. Analysis of the clay principle component and the biogenic silica component ($PC1_{10\text{-}sec}$ and $PC4_{10\text{-}sec}$) suggests there are discernable differences between the three selected core sections within these two principal components (Figure 3.3.3).

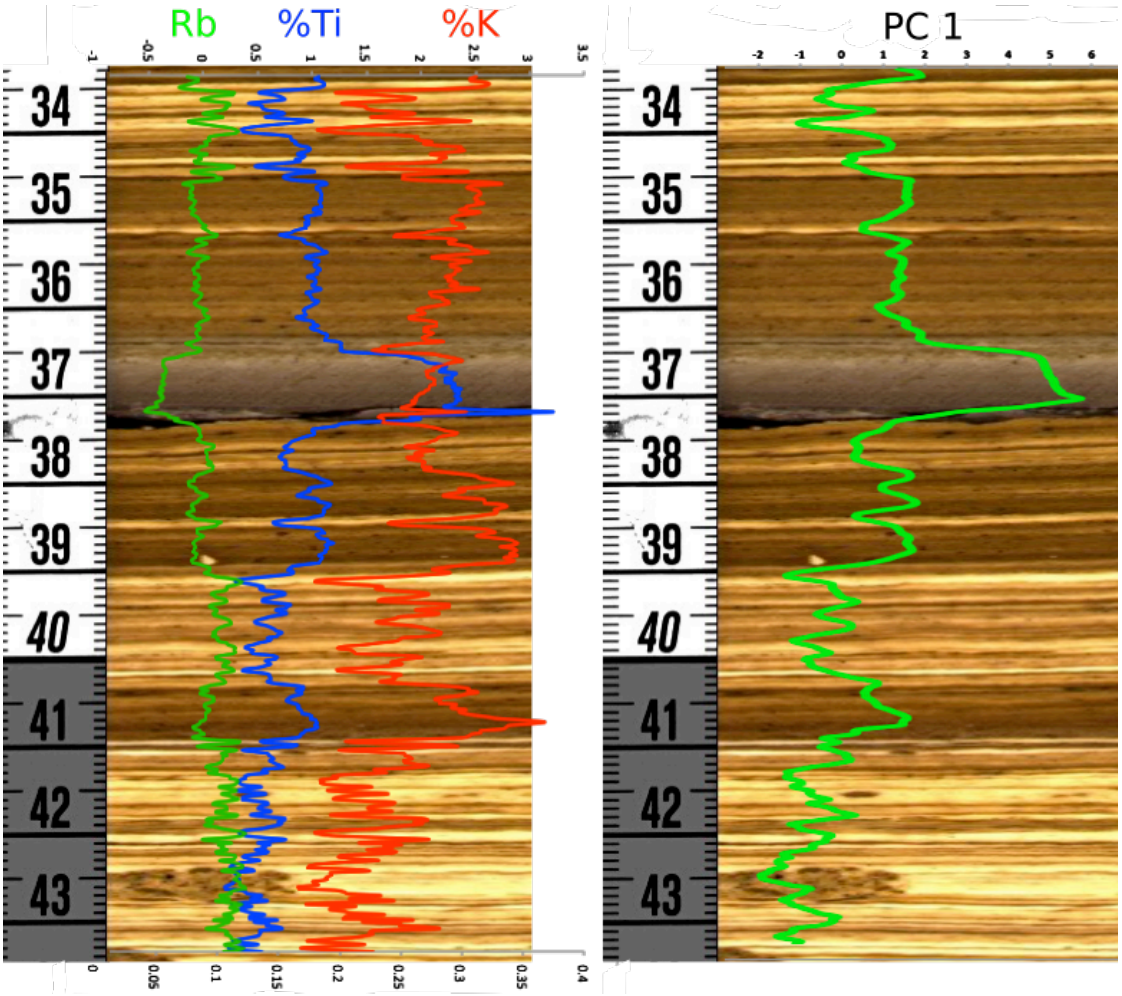

Figure 3.3.2: Element counts/percents vs. $PC1_{10\text{-}sec}$
Element counts (Rb) and percentages (%Ti, %K) overlain finely laminated sediment in comparison to $PC1_{10\text{-}sec}$

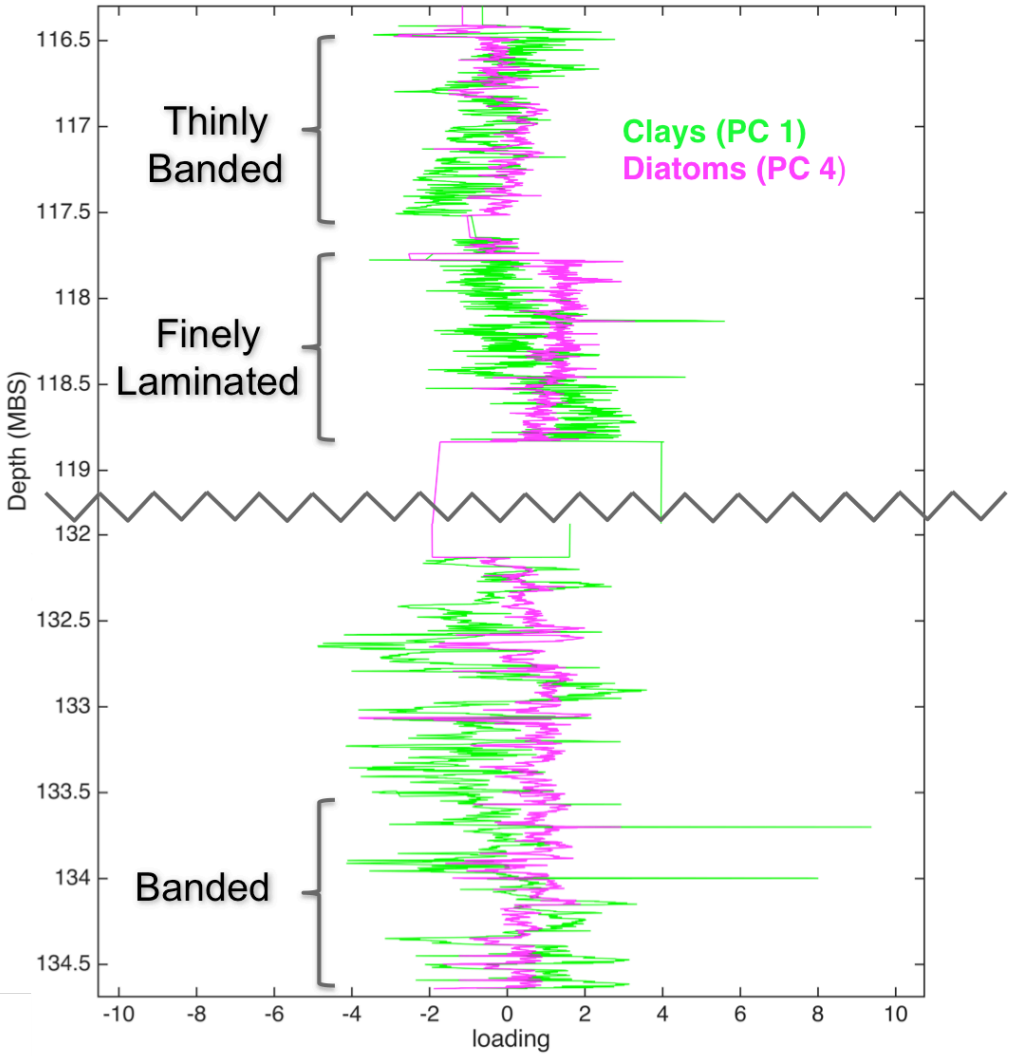

Figure 3.3.3: PC1, PC4 vs. MBS
$PC1_{10\text{-sec}}$ and $PC4_{10\text{-sec}}$ plotted with depth, three distinct core sections noted

In the thinly banded section, clays decline rapidly downcore and silica declines slightly but is less variable. Beneath the thinly banded sections, the finely laminated section has the opposite characteristics. The clays increase rapidly downcore and silica content also increases, but not as dramatically. In both of these core sections, the clay loading is higher than the silica component. Additionally, $PC1_{10\text{-sec}}$ and $PC4_{10\text{-sec}}$ appear to follow the same increasing or decreasing trend, but on a smaller scale, the clay and silica components are out

of phase with one another. The banded section is about 15m deeper in the core and is much more variable in both the clay and the silica components. In this section, the silica component is higher than the clay component.

3.4. Depositional Environments

XRF, optical and Scanning Electronic microscopy support that the 10 meters of sediment drill core chosen for analysis are lake sediments. However, lithological, elemental and mineralogical differences between the lacustrine core sections (e.g., banded, finely banded, finely laminated), suggest that these sediments accumulated in different lacustrine depositional environments. One major controlling factor of the formation and preservation of banded and laminated sediments is the water depth at times of deposition (Verschuren, 1999). The three different lithologies may reflect three different lake levels. The banded section, with its non-distinct terminations between bands and thick layers, is likely to have been deposited in a shallow lake system, wherein, sediments are often re-suspended via wind induced mixing, which destroys newly formed fine laminations (Verschuren, 1999). In contrast, in a deeper lake wind and wave energy does not propagate to the lake floor, so the sediments remain undisturbed and laminations are often preserved. The finely laminated section therefore indicates that the lake was deep at the time of sediment deposition. In this case, the fine laminations alternate between being diatomaceous and clay rich, pointing to the same type of seasonal deposition and preservation observed in Lake Challa (discussed in Chapter 4). The finely laminated section and the banded sediments represent two end members of the lacustrine system, deep and fresh versus shallow and alkaline, while the thinly banded section falls

between them and has characteristics more similar to the deep system in terms of layer thickness, lamination terminations, and microfacies characteristics.

Aside from band/lamination thickness and characteristics, another distinguishing characteristic between the three sections is calcite preservation, which can reflect lake level and whether a lake is an open or closed basin. In an open basin, dissolved ions that enter the basin from the catchment leave through surface outflow. In a closed basin, water only leaves the basin through evaporation, or through lakebed seepage into the groundwater. Evaporation does not remove any dissolved ions from the basin, which leads to an increase in ionic concentrations in lake water (Verschuren, 1999). Calcium carbonate precipitates in a water body when the water column is saturated with calcium and carbonate ions. While an open basin's surface outflow results in low ion concentrations, in a closed, alkaline basin ion saturation may lead to carbonate mineral precipitation in the water column and preservation in the sediment (Verschuren, 1999). In such cases, sediment records of calcite content may reflect changes from a closed to an open basin system.

Even in a closed basin, there can be different conditions that affect calcium carbonate precipitation and preservation. Calcium carbonate precipitates in oxic alkaline environments and dissolves in acidic conditions often linked to anoxic environments (Pompeani 2012). A deep, fresh lake in a closed basin could precipitate calcium carbonate in its shallow areas, only for it be dissolved in its bottom waters and thus not be preserved in the sediment. If the Olorgesailie paleolake was a closed basin throughout the examined interval, the relationship between lake level and calcium carbonate preservation could explain the low levels of calcium carbonate in the intermediate and deep lake sediments.

Another factor that affects calcium carbonate precipitation in a closed basin is hydraulic transmissivity. As lake level increases, so does the surface area of the lake floor (Fetter 2001). This increase in surface area typically

inundates sediments with a greater hydraulic conductivity, leading to an increase in water losses through the sediments by seepage (Heath 1983). At lower lake levels (volume) the hydraulic transmissivity of sediment inundated by a lake is typically lower, resulting in lower outflow through seepage (Heath 1983). With less water leaving through the sediments, a lower lake level in this case would lead to a higher salinity. This direct relationship between lake level and hydraulic conductivity could also explain the high concentration of calcium carbonate preservation in the shallow lake sediments and the relatively lesser amounts in the sediments deposited under the deep lake and intermediate lake environments.

3.5. Summary of the Microfacies Analysis

Ten core sections of lacustrine sediment were chosen from a 30m interval from the Olorgesailie drill cores for high resolution XRF and imagery analysis. Three of the ten core sections were selected to be subsampled and further analyzed based on their distinct banding or laminated characteristics. The three sections have discrete layer structure that is expressed in the XRF data and the optical and SEM imagery. In all three sections, the lighter layers have a higher biogenic silica content (Si:Ti) and the darker layers have a higher clay content (%Ti, %K). The calcium carbonate content varies between the three sections in both concentration and distribution.

The XRF elemental data closely follows the color and microfacies structural changes in the core sections. A principle component analysis indicates that the first two principle components, $PC1_{10\text{-}sec}$ and $PC4_{10\text{-}sec}$, which reflect clay as diatom concentration variability, respectively, capture 47% of the variance in

the 10-section data set. These principal components are helpful in distinguishing different sediment types from one another within the 10-section data set, but do not capture the inter-laminar variance as well as the elemental percentage based proxies.

The three sections appear to represent three different depositional environments. The banded section is interpreted to be characteristic of a shallow alkaline lacustrine environment where calcite is preserved in the sediment and annual layering is not preserved. The finely laminated section exhibits alternating clay and diatomaceous layers, indicating an annual record of seasonal changes in a deeper fresher lake. The thinly banded section suggest an intermediate lake depth, closer in layer thickness and sediment characteristics to the deep, fresh lake reflected by the finely laminated section, which notably lies directly adjacent and below this section of core. The finely laminated section and the thinly banded section contain far less calcite than the thinly banded and banded sections.

The microfacies analysis provides critical ground truthing for relating the XRF data to compositional characteristics of the sediment. Microfacies analysis was conducted on only four subsamples from the 10 core sections. While the subsamples were chosen based on ~8cm core sections thought to be representative of the overall core stratigraphy, extrapolating the information from those small samples to the larger sections and further to the whole 10-core suite was a qualitative exercise. However, the strong relationship between the XRF elemental data and structure identified via microscopic imagery analysis lends support to this projection of microfacies results to the entire core suite.

4. Focusing on the Fine Laminations

4.1. Lake Challa: A Modern Analog to Olorgesailie

Presently, East African seasonality is characterized by the long rain season and the short rain season, with dry seasons in between (Wolff 2014). Although East Africa is much drier today than it was during the time interval of the Olorgesailie paleolake (200-400ka), there are lakes in the region that may be modern analogs of seasonal changes in lake chemistry. Lake Challa, located at the base of Mt. Kilimanjaro and only 240 km miles away from Olorgesailie, may provide insights how the lake at Olorgesailie might have behaved.

Lake Challa's varved sediments have been analyzed and compared with seasonally monitored sediment traps (Figure 4.1.1). During the austral summer (November – March), the temperature rises and the ICTZ moves southward over the region, bringing precipitation with it. During this time Lake Challa is warmer, biologically productive with non-diatom algae, and experiences high calcite precipitation in the water column. This distinct seasonal lake geochemistry is expressed in the varved sediment in the dark as dark layers, predominantly consisting of amorphous organic matter with some endogenic calcite (Wolff 2011). In between the austral summer and winter (March thru May), the ITCZ sweeps back over the region as it approaches its northern position. This northern passage of the ITCZ brings the long rains, flushing clays from the catchment into the lake. These clays are recorded in the sediment as part of the dark layers in the varved couplets (Wolff 2011). During the austral winter (May - August), the

ITCZ migrates north, producing high winds and cooler temperatures. This increase in wind causes major upwelling in Lake Challa, resulting in diatom blooms in the water column, which are also recorded in the sediment as light layers (Wolff 2014, 2011). The amount of precipitation during the short rains (October thru December) are much more variable.

These dry and wet season cycles have been tied to the El Nino-Southern Oscillation (ENSO) and Indian Ocean dipole (IOD) using cores from Lake Challa, East African climate observations, and modeling (Wolff 2011, 2014, Marchant 2007). The IOD is characterized by east-west oscillation of warm sea surface waters in the Indian Ocean. The positive dipole mode, when the warm sea surface waters migrate westward toward Africa, results in increased convective activity and thus heavy rainfall over East Africa (Marchant 2007). The negative dipole mode, when the warm waters migrate eastward toward and increase convective activity over Indonesia and Australia, inducing inverse conditions in East Africa (Marchant 2007). The exact relationship between the IOD and ENSO has been contested, but there is wide agreement that ENSO has some degree of influence on sea surface temperatures (SSTs) in the Indian Ocean (Marchant 2007).. There is evidence that in the last 100 years, ENSO has had a dynamic interaction with Indian ocean SSTs and thus regional climate variability, with the interaction varying more broadly over Holocene records (Sandweiss et al., 2001, Marchant et al. 1999), indicating an even greater variation extending back in geologic history (Marchant 2007). However, whether the driver is understood, regional rainfall is intrinsically tied to local SSTs through the dynamics of convective activity and precipitation (Marchant 2007).

Present conditions of the effect of ENSO on East African climate have been recorded in Lake Challa's modern sediment as variations in varve thickness. In La Nina conditions, the dry season in East Africa is windier, and the short rains are more variable. The greater wind speed during these years cause

greater upwelling of nutrient dense bottom water, leading to large diatom blooms, leaving a thicker light colored layer in the sediment (Wolff 2011). In El Nino conditions, the climate in East Africa is wetter and less windy during the short rain season, leading to less upwelling of the bottom water and a smaller that average diatom bloom, leaving a thinner light lamination in the sediment (Wolff 2011).

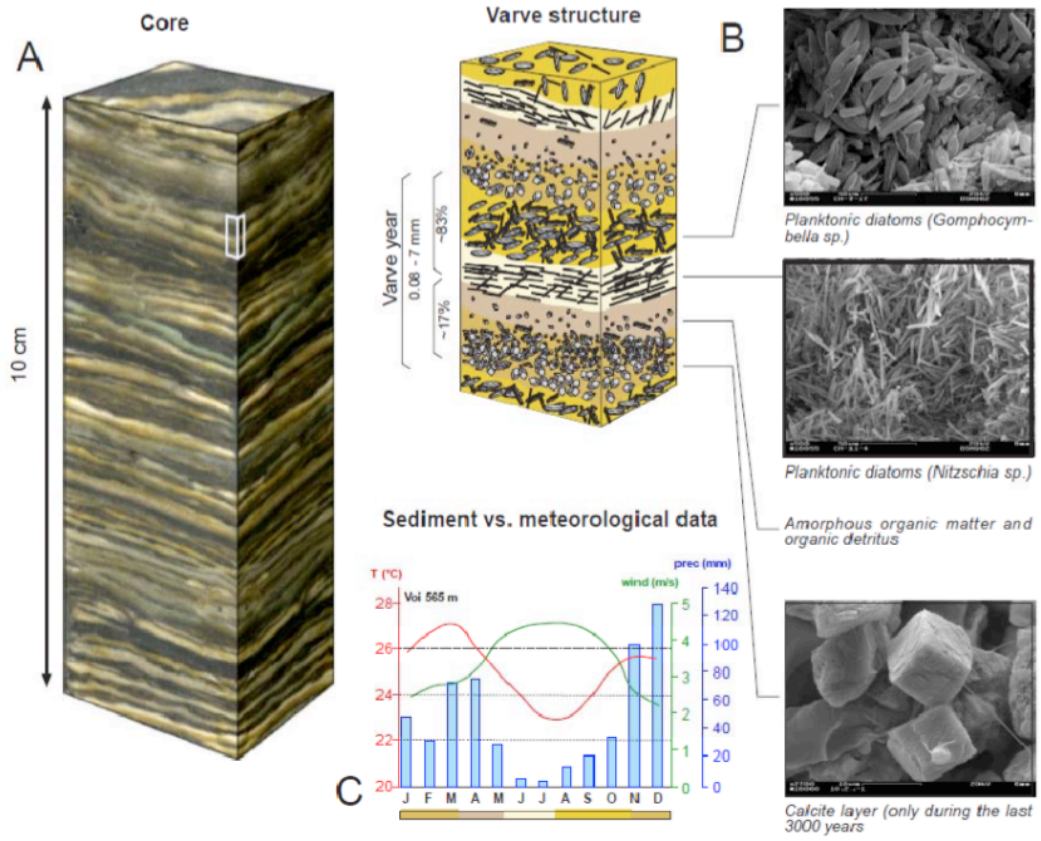

Fig.S4. Structure of finely laminated Lake Challa sediments. (**A**) Lake Challa sediment column showing the succession of light and dark layers. (**B**) Microfacies analyses reveal that the dark layers predominantly consist of amorphous organic matter and crystals of endogenic calcite. Diatom frustules are the overall dominant constituents of the light layer. Light layers are usually the most prominent, ranging from 20% to 99.7% (mean 83%) of total varve thickness in the two studied sections, whereas the dark layers range from 0.3% to 80% (mean 17%). (**C**) Comparison of the respective light and dark layer components collected in monthly sediment-trap samples (coloured bar) with meteorological data from Voi (80 km east of Lake Challa, Kenya) allows us to connect the dark layer to the warm and wet southern hemisphere summer and the light diatom layer to the cool, dry and windy southern hemisphere winter. We therefore interpret each light/dark couplet as a varve, representing one full year of lacustrine sedimentation.

Figure 4.1.1: Lake Challa's varved sediment structure
Microfacies analysis linked with annual precipitation and temperature (Wolff 2011 Supporting Online Materials)

4.2. Principal Component Analysis: revisited

The Principal component analysis (PCA) run on the 10 core sections ($PCA_{10\text{-}sec}$) was useful in the larger scale, examining the whole 10-core suite, but not as useful for laminar examinations. In order to quantify elemental data from the finely laminated section, the same PCA procedure was followed, using only data from core section ODP-OLO12-2A-63Q-2 ($PCA_{1\text{-}sec}$, the finely laminated section).

Similar to $PCA_{10\text{-}sec}$, $PC1_{1\text{-}sec}$ and $PC2_{1\text{-}sec}$ represent variations between clays and calcium carbonate content (Figure 4.2.1). In this smaller data set, $PC1_{1\text{-}sec}$ and $PC2_{1\text{-}sec}$ capture almost 80% of the variance (Table 1). Elements associated with clay composition load positively on $PC1_{1\text{-}sec}$, with K, Ti, Fe, Zr, and Rb loading distinctly out of phase with Si, which loads negatively (Figure 4.2.1). Carbonate elements (Ca and Sr) load positively and all other elements value near zero in $PC2_{1\text{-}sec}$ (Figure 4.2.1). Another difference between $PCA_{1\text{-}sec}$ and the $PCA_{10\text{-}sec}$ is the third and the fourth components are switched. In $PCA_{10\text{-}sec}$, $PC4_{10\text{-}sec}$ represents the silica component; whereas in this analysis, $PC3_{1\text{-}sec}$ captures the silica component (Figure 3.3.1). The third and fourth principle components in this analysis capture 18% of the variance combined, compared to 22% in $PCA_{10\text{-}sec}$ (Figure 4.2.1, Figure 3.3.1).

Principal Component	PC 1	PC 2	PC 3	PC 4	PC 5	PC 6	PC 7	PC 8	PC 9
Eigen values	0.57	0.17	0.10	0.08	0.05	0.01	0.01	0.003	0.002

Table 1: Normalized Eigen values for PCA on section 63Q-2

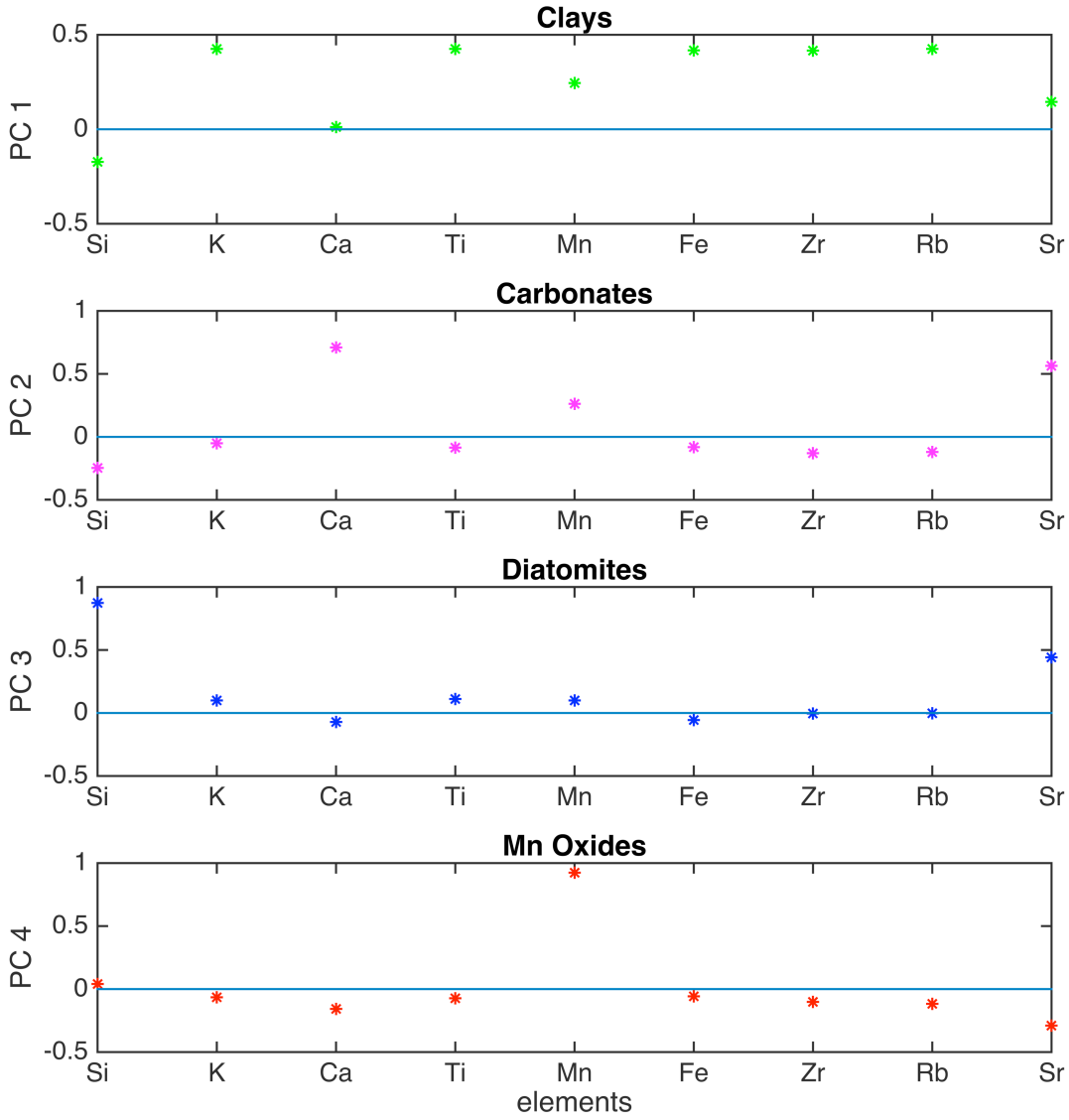

Figure 4.2.1: $PC_{1\text{-sec}}$ Element loadings

The clay component from $PCA_{10\text{-sec}}$ generally follows the lamination changes but does not capture laminations thinner than 2-3mm. $PC1_{1\text{-sec}}$ captures these mm-scale changes more accurately (Figure 4.2.2). Not only does $PC1_{1\text{-sec}}$ capture the millimeter scale variations, but also it also generally follows overall color shifts in the core, exhibiting greater values in the darker sections and lesser values in the lighter sections (Figure 4.2.3).

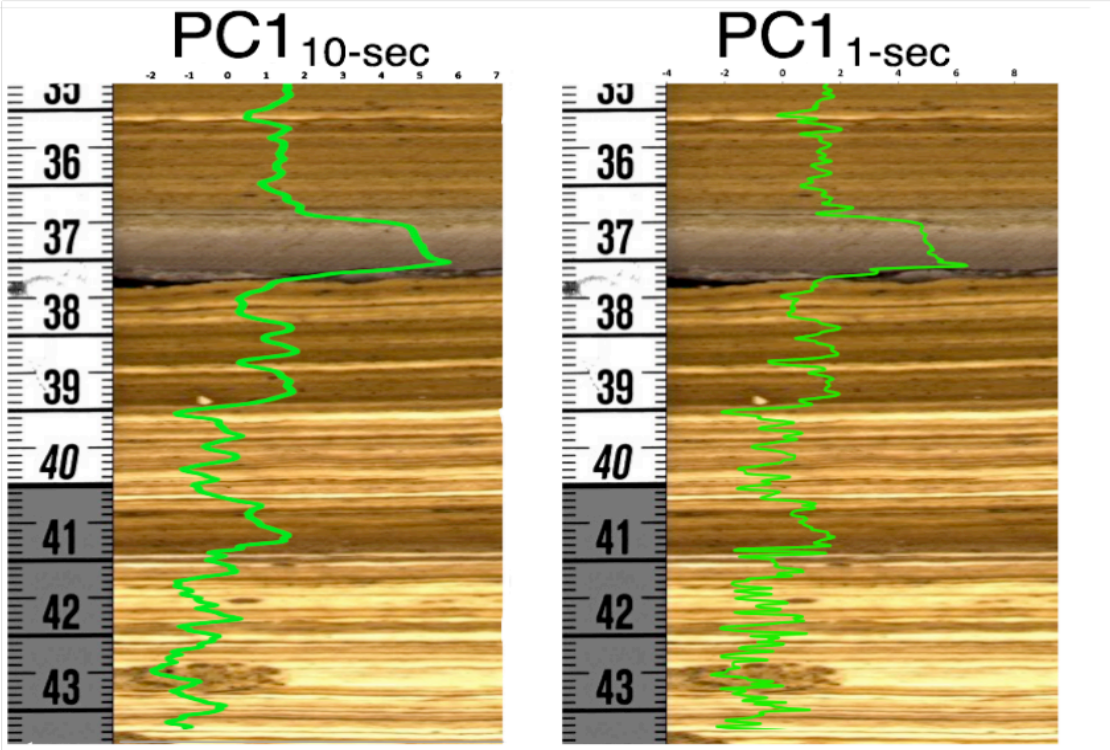

Figure 4.2.2: $PC1_{10\text{-}sec}$ versus $PC1_{1\text{-}sec}$ over 63Q-2 core image

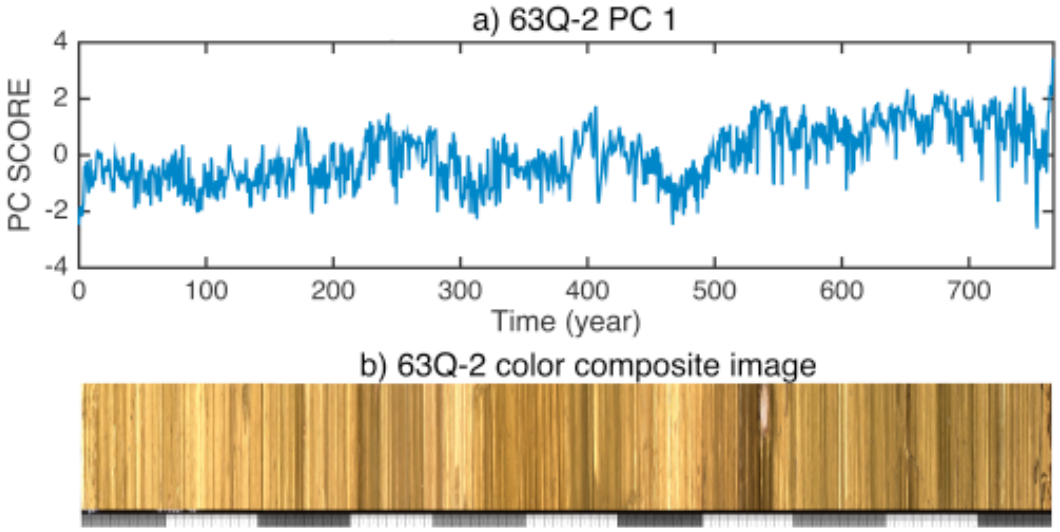

Figure 4.2.3: $PC1_{1\text{-}sec}$ and 63Q-2 image

a) $PC1_{1\text{-}sec}$ on core section 63Q-2, with the age model from the BMPix/PEAK macros. b) Composite image of the scanned section of core, with tephras removed. Age on top figure matches depth on bottom image.

4.3. Wavelet analysis on PC 1

Wavelet power spectrum analysis determines the strength of periodicities in a time series. Wavelet power spectral analysis was performed on the $PC1_{1\text{-sec}}$ from the short data set using an adapted MATLAB script (Torrence 1998). The wavelet power spectrum (Figure 4.3.1, b) on the raw, unfiltered data from PC1 shows a strong significance within the 100-160 year frequency range, as indicated by the global wavelet spectrum (Figure 4.3.1, c). Two filters, a 50-year high pass and a 50 year low pass, were applied to the data set in order to examine the high and low frequency spectral powers.

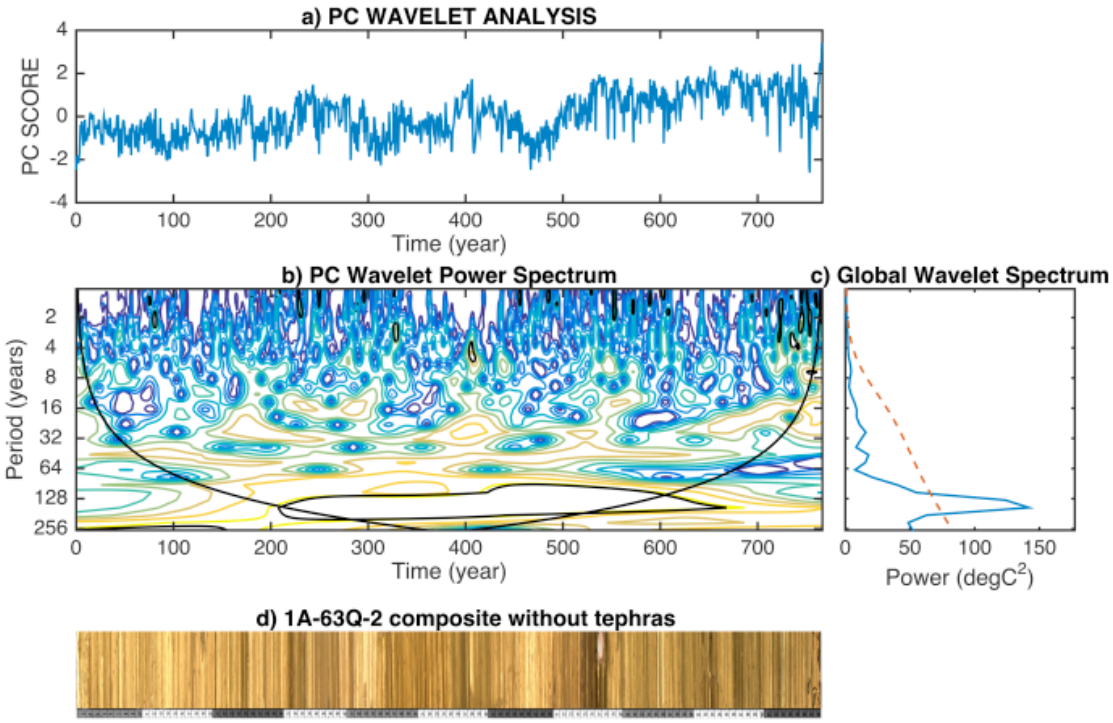

Figure 4.3.1: PC 1 Wavelet Analysis, Unfiltered
(a) $PC1_{1\text{-sec}}$ on the BMPix/PEAK age model interpolated at 0.5 years, unfiltered. (b) Wavelet power spectrum of $PC1_{1\text{-sec}}$, thick black line marking cone of influence at 95% significance. (c) Global wavelet spectrum, with red dashed line marking 95% significance. (d) Color composite image of scanned area of core 2A-63Q-2, with tephras removed.

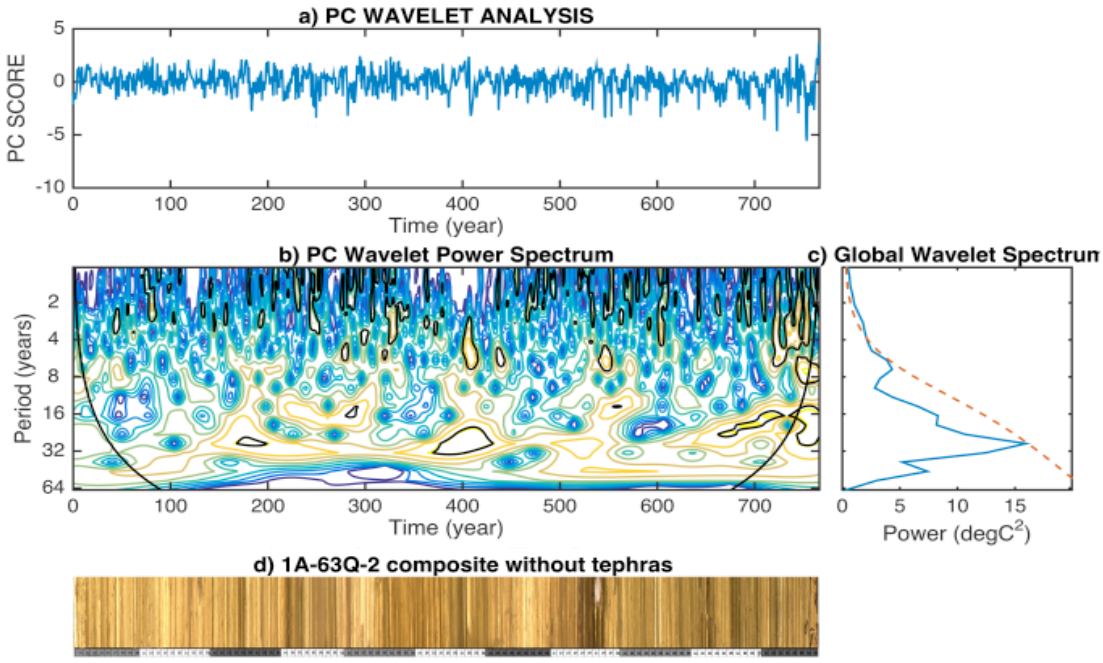

Figure 4.3.2: PC 1 Wavelet Analysis, 50-yr High Pass
(a) $PC1_{1\text{-sec}}$ on the BMPix/PEAK age model interpolated at 0.5 years and high passed filtered (50-year). (b) Wavelet power spectrum of $PC1_{1\text{-sec}}$, thick black line marking cone of influence at 95% significance. (c) Global wavelet spectrum, with red dashed line marking 95% significance. (d) Color composite image of scanned area of core 2A-63Q-2, with tephras removed.

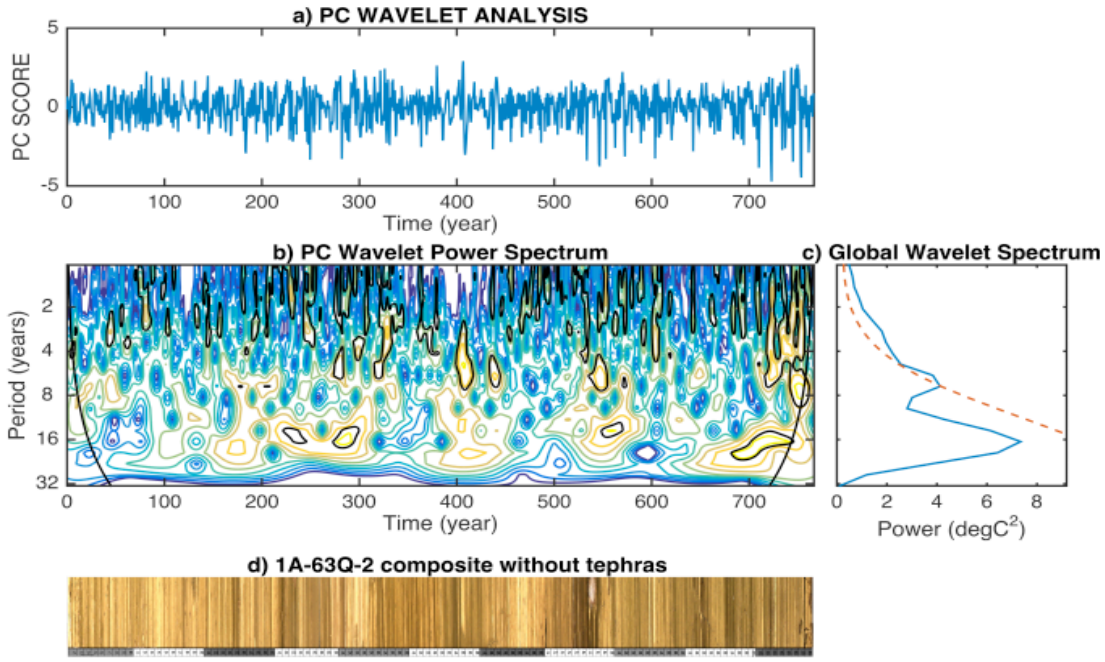

Figure 4.3.3: PC 1 Wavelet Analysis, 25-yr High Pass
(a) $PC1_{1\text{-sec}}$ on the BMPix/PEAK age model interpolated at 0.25 years and high pass filtered (25-year). (b) Wavelet power spectrum of $PC1_{1\text{-sec}}$, thick black line marking cone of influence at 95% significance. (c) Global wavelet spectrum, with red dashed line marking 95% significance. (d) Color composite image of scanned area of core 2A-63Q-2, with tephras removed.

There is a significant peak around the 128-year frequency range of the unfiltered data, very close to the cone of influence (Figure 4.3.1). There are higher frequencies that exhibit significance in the global wavelet spectrum, but they are hard to identify in the analysis of the unfiltered data. All frequencies below 50-years were removed with the 50-year high pass filter (Figure 4.3.2). Frequencies between 4-8 years and at 25-28 years in the global wavelet spectrum are significant (panel c, Figure 4.3.2). To assess the robustness of this result, the data were interpolated at 0.25 years and high pass filtered at a 25-year frequency (Figure 4.3.3). Both the peak between 4 and 8 years frequency and the 25 to 28-year frequencies are much more pronounced in this analysis (c, Figure 4.3.3). A 50-year low pass filter was applied to the data to examine the peak in the lower frequency range in the unfiltered data (c, Figure 4.3.1). The

low-pass filtered data shows a significance around the 128-year frequency, but it is so close to the cone of influence that this result may not be valid.

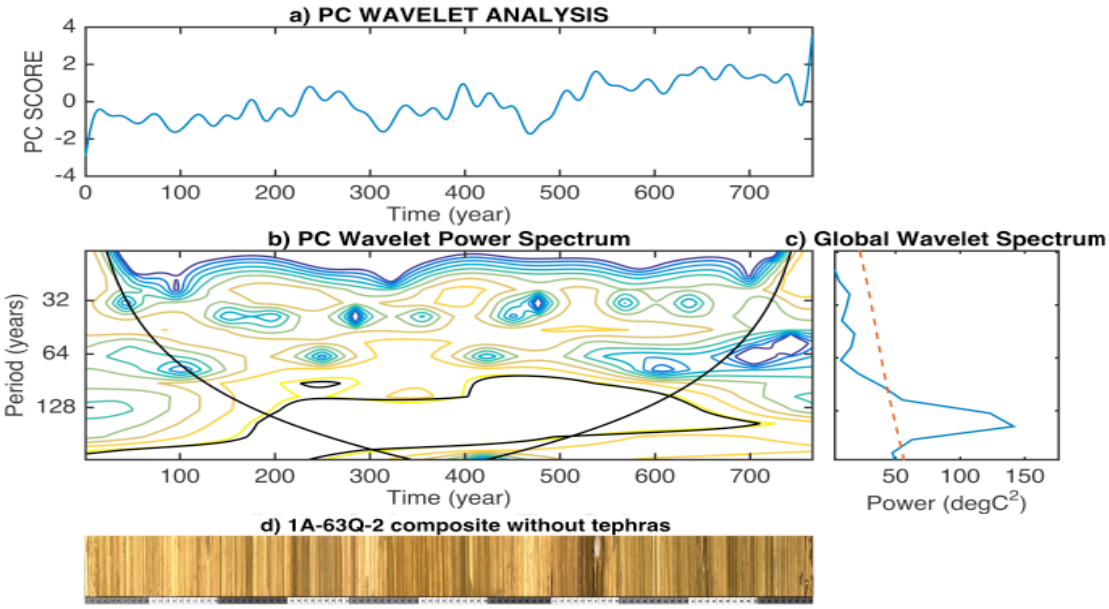

Figure 4.3.4: PC 1 Wavelet Analysis, 50-yr Low Pass
(a) $PC1_{1\text{-}sec}$ plotted against BMPix/PEAK age model interpolated at 0.5 years and low pass filtered (25-year). (b) Wavelet power spectrum of $PC1_{1\text{-}sec}$, thick black line marking cone of influence at 95% significance. (c) Global wavelet spectrum, with red dashed line marking 95% significance. (d) Color composite image of scanned area of core 2A-63Q-2, with tephras removed.

4.4. Varve thickness wavelet comparisons

Wavelet spectral analysis was also performed on varve thickness data from the core section 63Q-2. Varve thickness data from modern and last glacial maximum (LGM) sections of Lake Challa sediment cores were subject to the same analysis for comparison (Wolff 2011).

The unfiltered OLO varve thickness wavelet spectral analysis exhibits significant power in frequencies less than 10 years, specifically the 4-8 year frequency range (Figure 4.4.1). The Challa modern varve thickness exhibits

spectral power in the 1-6 year frequency range (Figure 4.4.2). The global wavelet spectrum from the OLO varve thickness data looks most similar to the Challa modern varve thickness than the Challa LGM varve thickness spectral analysis. The Challa LGM varve thickness data also has significant high frequency spectral power, but the global wavelet spectrum is distinctly different from the other two data sets, with much lower spectral power in the high frequency range (Figure 4.4.3).

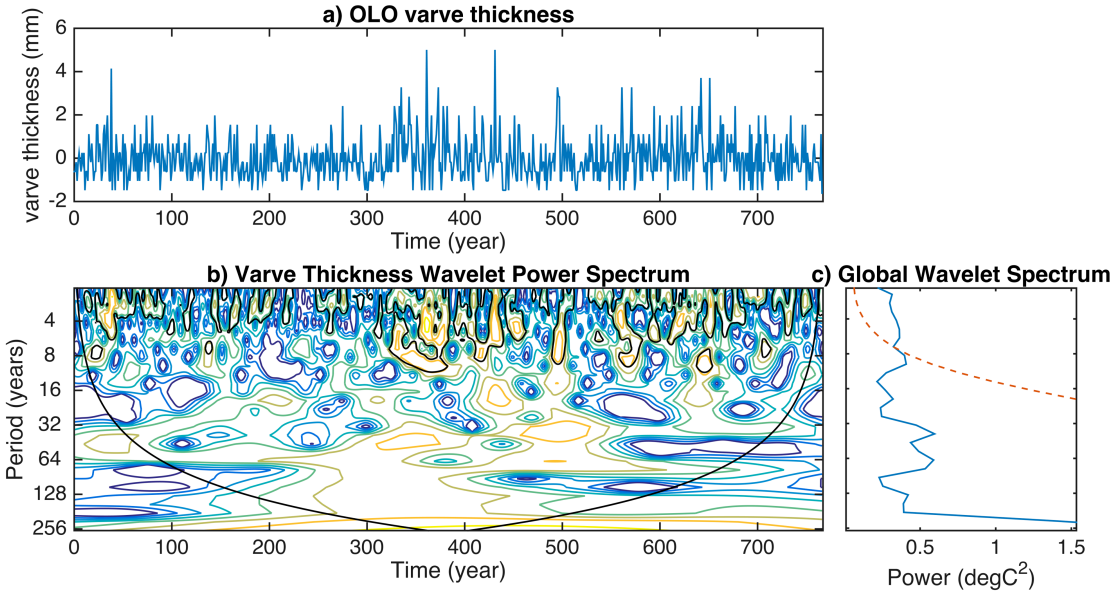

Figure 4.4.1: OLO Wavelet Analysis, Unfiltered
(a) OLO varve thickness on the BMPix/PEAK age model interpolated at 0.5 years. (b) Wavelet power spectrum of OLO varve thickness, thick black line marking cone of influence at 95% significance. (c) Global wavelet spectrum, with red dashed line marking 95% significance.

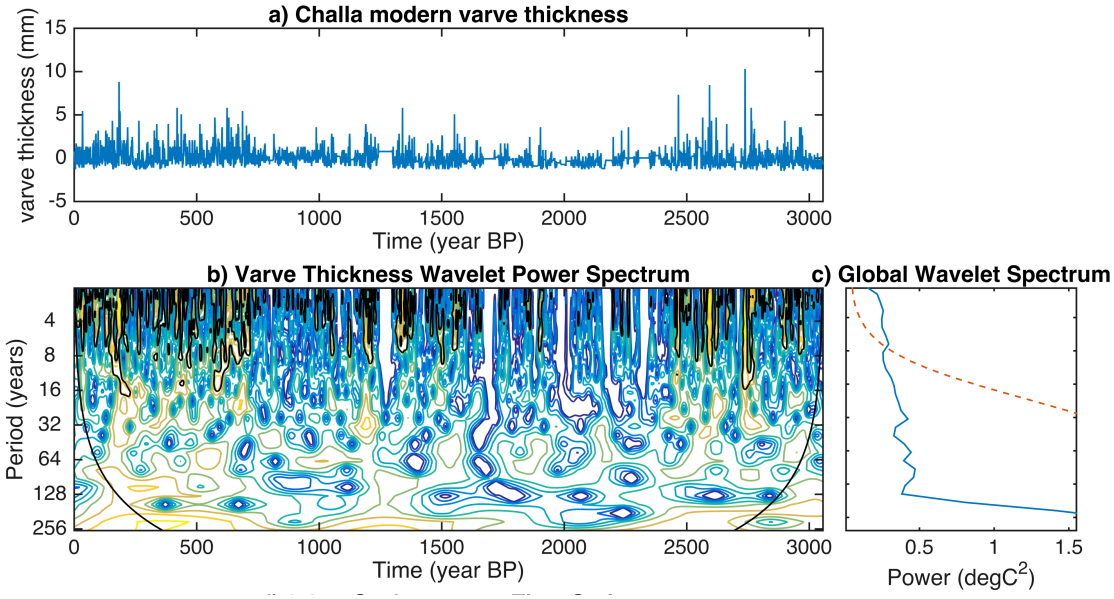

Figure 4.4.2: Challa Modern Wavelet Analysis, Unfiltered

(a) Challa modern varve thickness plotted against age (year BP) interpolated at 0.5 years. (b) Wavelet power spectrum of Challa modern varve thickness, thick black line marking cone of influence at 95% significance. (c) Global wavelet spectrum, with red dashed line marking 95% significance.

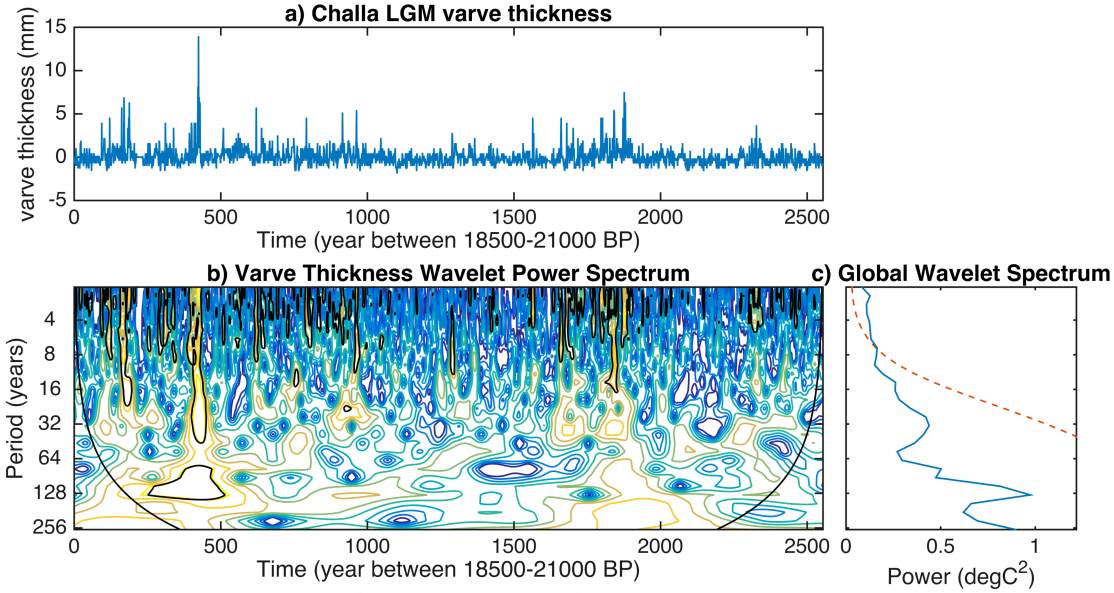

Figure 4.4.3: Challa LGM Wavelet Analysis, Unfiltered

(a) Challa LGM varve thickness plotted against age (years between 18.5-21 kyr BP) interpolated at 0.5 years. (b) Wavelet power spectrum of Challa LGM varve thickness, thick black line marking cone of influence at 95% significance. (c) Global wavelet spectrum, with red dashed line marking 95% significance.

A 50-year low pass filter was applied to the data sets in order to examine low frequency spectral power. In the OLO varve thickness data exhibits significant power in the 50-75-year frequency range (Figure 4.4.4). There is a small peak around 128-year frequency, and a larger peak below the cone of influence (Figure 4.4.4). In the modern Challa varve thickness data, the low frequency peaks are around 50-75 years, 100-years, and between the 150-300 year frequency ranges (Figure 4.4.5). The Challa LGM varve thickness data has a peak around 100-years, the 200-years, and between 300-500 years (Figure 4.4.6). The overall shape of the low-pass filtered global wavelet spectrum for the OLO varve thickness data is more similar to the Challa modern varve thickness data than it is to the Challa LGM varve thickness data.

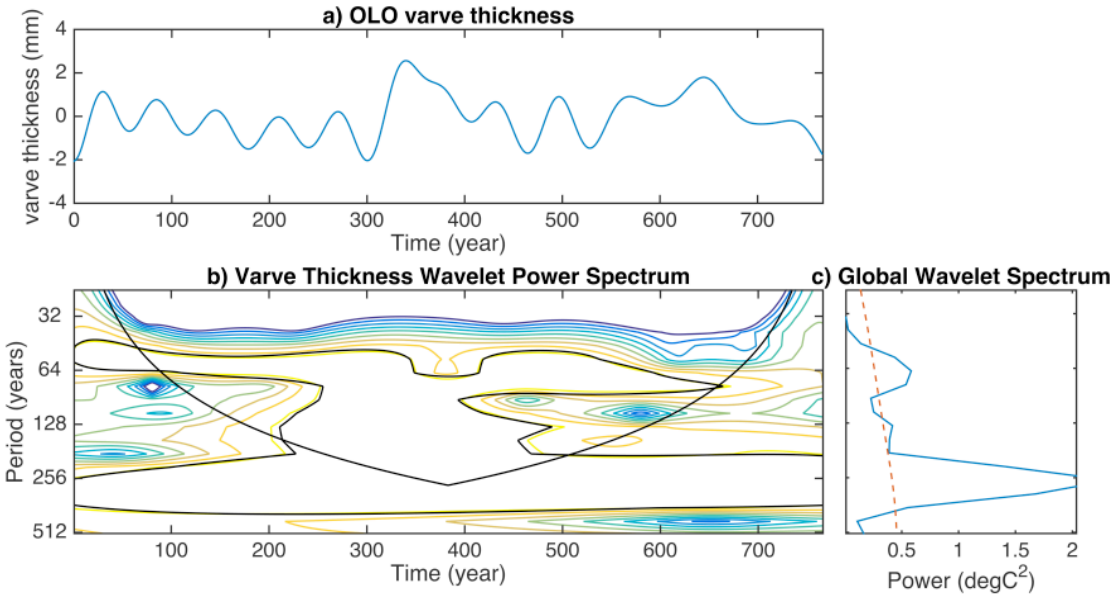

Figure 4.4.4: OLO Wavelet Analysis, 50-yr Low Pass
(a) OLO varve thickness on the BMPix/PEAK age model interpolated at 0.5 years, low pass filtered (50-years). (b) Wavelet power spectrum of OLO varve thickness, thick black line marking cone of influence at 95% significance. (c) Global wavelet spectrum, with red dashed line marking 95% significance.

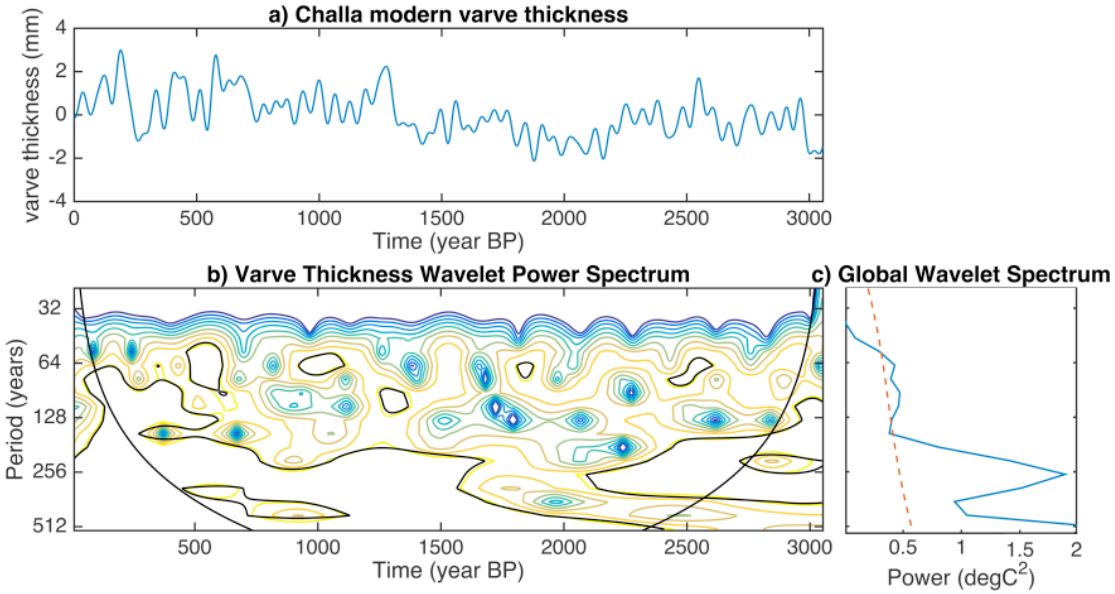

Figure 4.4.5: Challa Modern Wavelet Analysis, 50-yr Low Pass
(a) Challa modern varve thickness plotted against age (year BP) interpolated at 0.5 years, low pass filtered (50-years). (b) Wavelet power spectrum of Challa modern varve thickness, thick black line marking cone of influence at 95% significance. (c) Global wavelet spectrum, with red dashed line marking 95% significance.

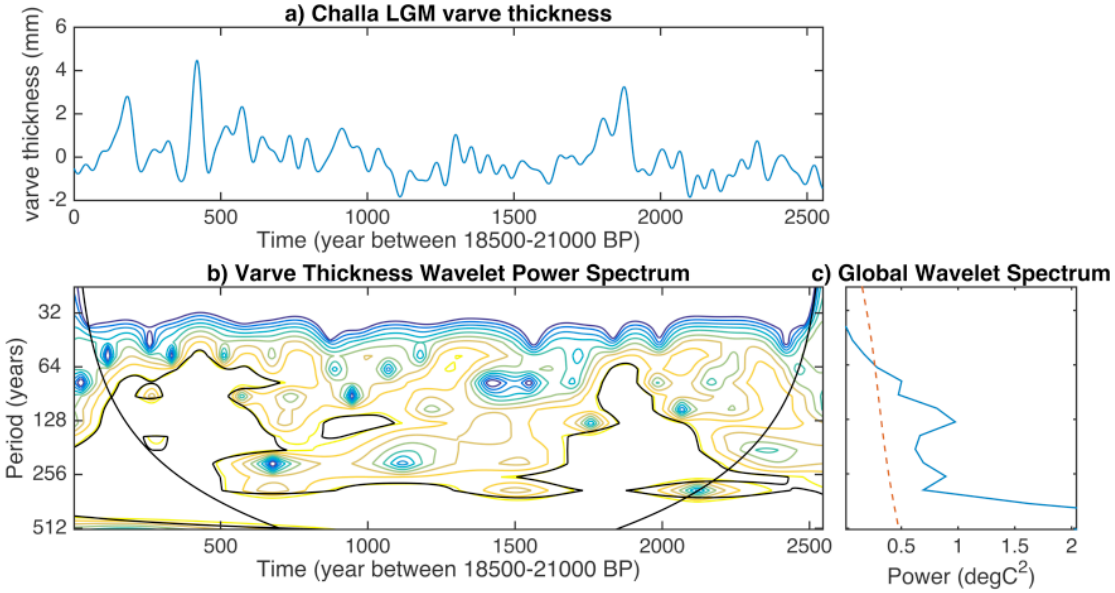

Figure 4.4.6: Challa LGM Wavelet Analysis, 50-yr Low Pass
(a) Challa LGM varve thickness plotted against age (years between 18.5-21 kyr BP) interpolated at 0.5 years, low pass filtered (50-year). (b) Wavelet power spectrum of Challa LGM varve thickness, thick black line marking cone of influence at 95% significance. (c) Global wavelet spectrum, with red dashed line marking 95% significance.

A 50-year high pass filter was applied to all three data sets in order to investigate high frequency spectral power. In the OLO varve thickness data global wavelet spectrum, there is significance in frequencies under 10 years, with strong peaks around the 6-year and the 10-year frequencies (panel c, Figure 4.4.7). There is also a peak at the 20-year frequency, but it is does not cross the 95% significance line. There are similar peaks in the Challa modern varve thickness global wavelet spectrum, offset at a slightly higher frequency. The peaks are around the 4-year and 8-year frequencies (panel c, Figure 4.4.8). In the Challa LGM global wavelet spectrum, there is a small peak near 1-year-frequency and another at the 8-year frequency. The higher frequencies in this data are not significant to as high a power on the global wavelet spectrum as the high frequencies in Challa modern and OLO (Figure 4.4.9).

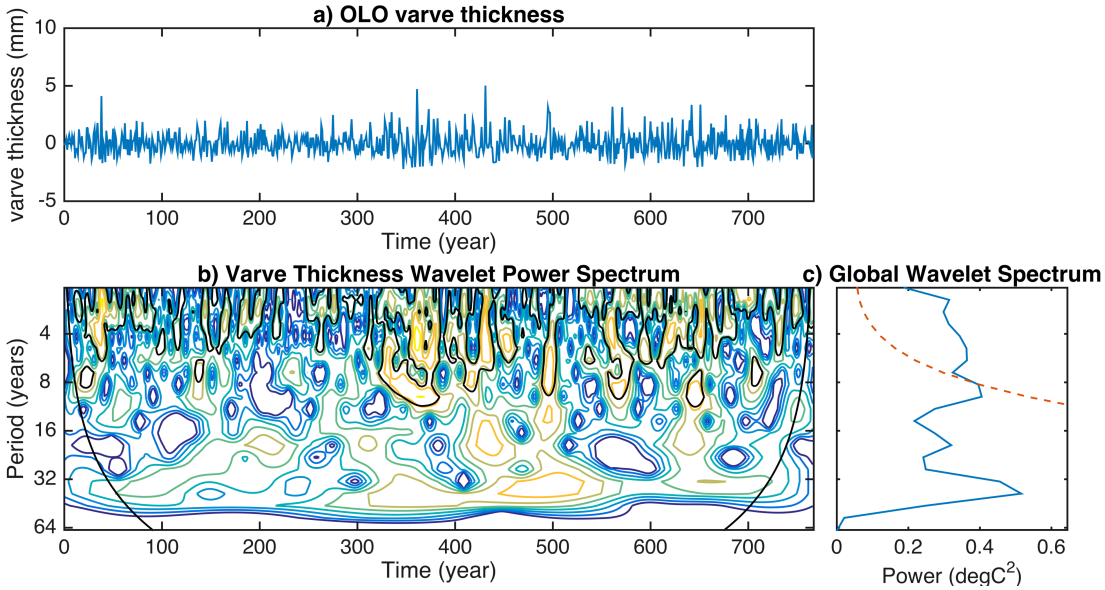

Figure 4.4.7: OLO Wavelet Analysis, 50-yr High Pass
(a) OLO varve thickness on the BMPix/PEAK age model interpolated at 0.5 years high pass filtered (50-year). (b) Wavelet power spectrum of OLO varve thickness, thick black line marking cone of influence at 95% significance. (c) Global wavelet spectrum, with red dashed line marking 95% significance.

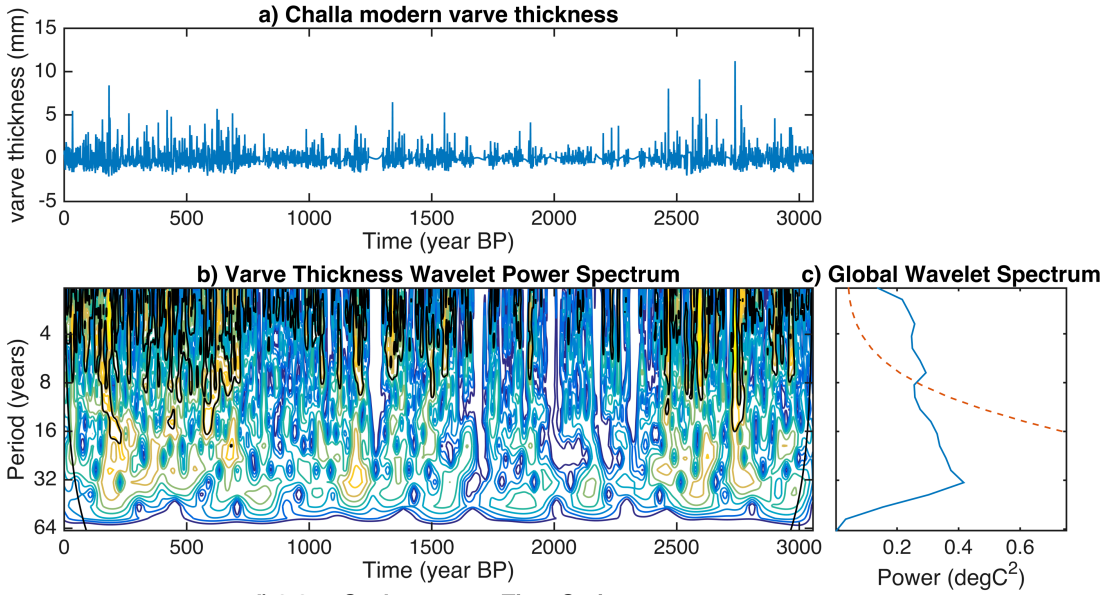

Figure 4.4.8: Challa Modern Wavelet Analysis, 50-yr High Pass

(a) Challa modern varve thickness plotted against age (year BP) interpolated at 0.5 years, high pass filtered (50-year). (b) Wavelet power spectrum of Challa modern varve thickness, thick black line marking cone of influence at 95% significance. (c) Global wavelet spectrum, with red dashed line marking 95% significance.

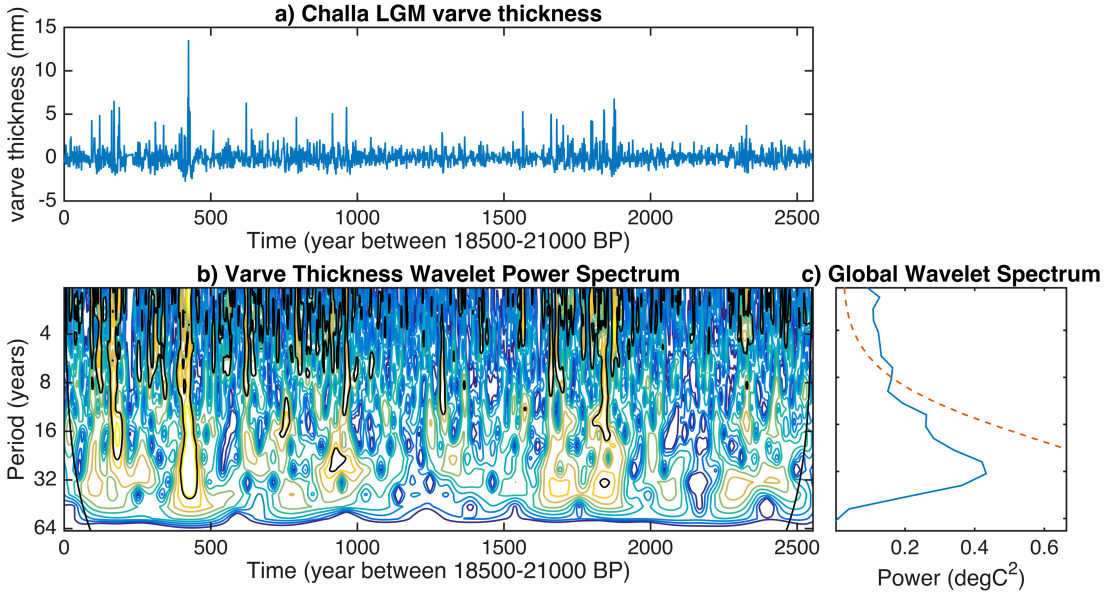

Figure 4.4.9: Challa LGM Wavelet Analysis, 50-yr High Pass

(a) Challa LGM varve thickness plotted against age (years between 18.5-21 kyr BP) interpolated at 0.5 years, high pass filtered (50-year). (b) Wavelet power spectrum of Challa LGM varve thickness, thick black line marking cone of influence at 95% significance. (c) Global wavelet spectrum, with red dashed line marking 95% significance.

Simple multi-taper method spectral analysis on the unfiltered varve thickness data from each data set was performed in order to better examine the high frequencies. Both OLO and Challa modern varve thicknesses exhibit significance at multiple frequencies between 3 – 10 years (Figure 4.4.10, Figure 4.4.11). OLO varve thickness shows significance at the 10-year, 6-year, 5.5-year, and 4-year frequencies (Figure 4.4.10). Challa modern varve thickness exhibits significance at the 9-year, 6-year, 5-year, 4.5-year, and around 3-year frequencies (Figure 4.4.11). While these two spectral analyses are not identical, the OLO and Challa modern varve thickness data are more similar than they are to the Challa LGM varve thickness spectral analysis. In the Challa LGM varve thickness data, there is only significance at the 5-year and the 2-year frequencies (Figure 4.4.12).

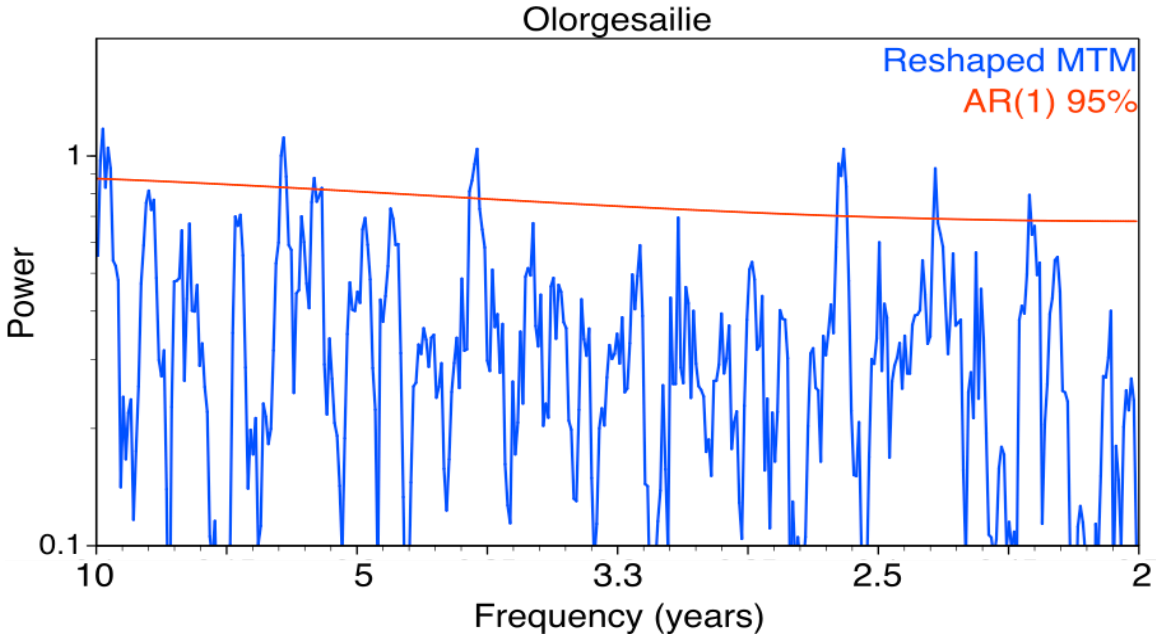

Figure 4.4.10: OLO High Frequency Analysis
OLO varve thickness spectral analysis (blue), with red line marking 95% significance.

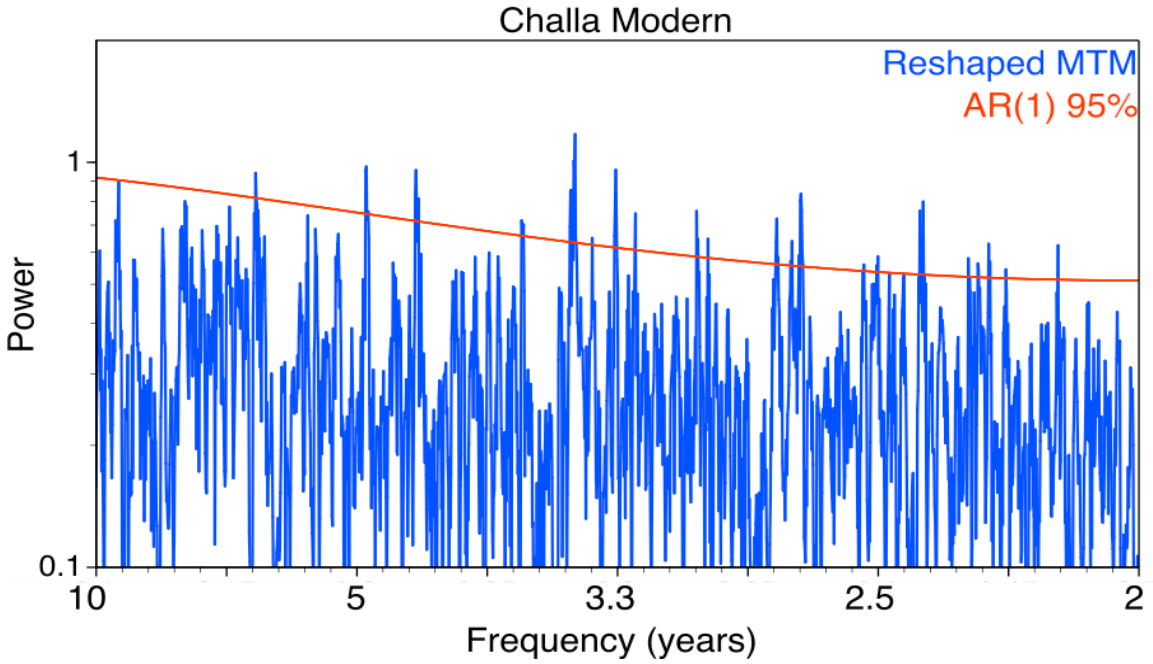

Figure 4.4.11: Challa Modern High Frequency Analysis
Challa modern varve thickness spectral analysis (blue), with red line marking 95% significance.

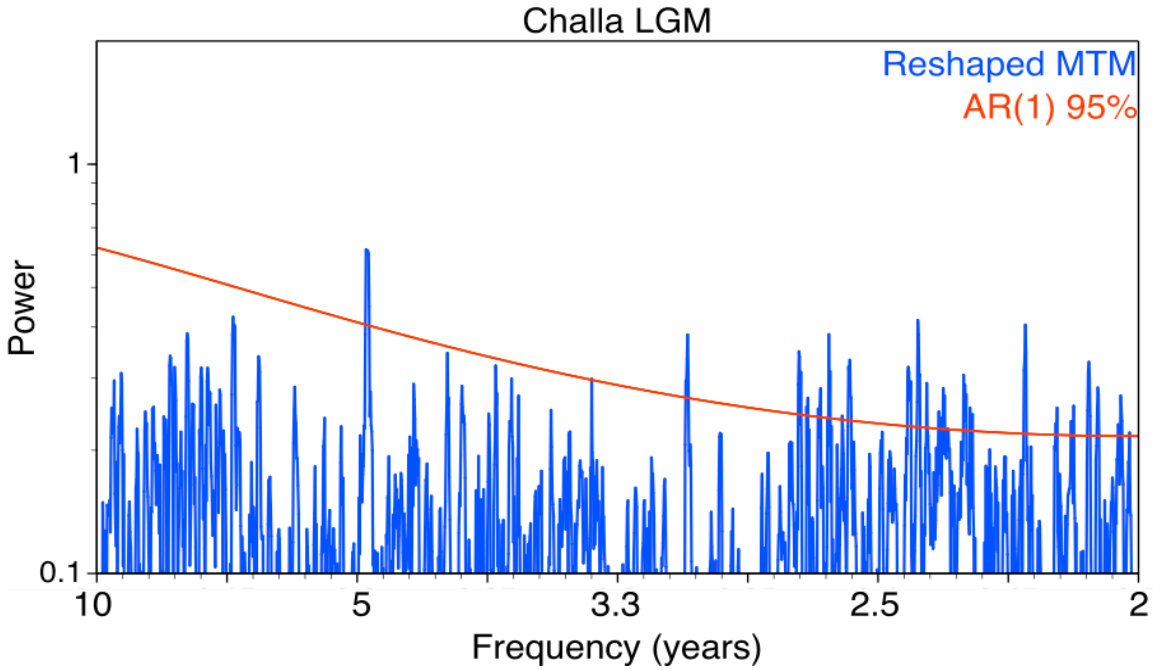

Figure 4.4.12: Challa LGM High Frequency Analysis
Challa LGM varve thickness spectral analysis (blue), with red line marking 95% significance.

4.5. Fine Laminations Conclusions

The spectral wavelet analysis performed on PC 1 of the finely laminated section of core reveals a few significant signals in the data. There is a significant 4-8-year signal, which is also evident in the OLO varve thickness analysis. This inter-annual signal in the OLO core section could be a result of ENSO like climate variability, which is a strong control on the modern Lake Challa system, as determined through analysis of modern varves and sediment trap samples (Wolff 2014, Wolff 2011). There is a peak in the 20-year frequency range in the $PC1_{1\text{-}sec}$ and OLO varve thickness data, although it is not significant in the latter. This multi-decadal signal in the $PC1_{1\text{-}sec}$ could be evidence of the 22-year solar cycle. The 22-year solar cycle has an observed effect on the modern Indian Ocean monsoon, and has been recorded in stalagmite paleoclimate records from central Asia during the LGM (Han et al. 2016).

There are similarities between the modern Lake Challa varves and the OLO core section 63Q-2 varves. As previously discussed in Chapter 3: Microfacies Analysis, there is evidence that this section of core was deposited in a deep, fresh lacustrine system in the Olorgesailie basin. The similarities between this section's wavelet analysis and the modern Challa wavelet analysis support this conclusion. Both clay content and varve thickness are affected directly by climate variability. Wetter years will flush more clay from the catchment into the basin, increasing the clay content in that lamination. Drier conditions are associated with greater wind speeds in East Africa (Wolff 2011), increasing upwelling in a deep lake with nutrient dense bottom water. In Lake Challa, these conditions lead to increased diatom blooms and thicker light laminations in the varved sediment. The similarities between the OLO varve thickness wavelet spectral analyses and the Challa modern varve thickness

analyses suggest that perhaps the deep Olorgesailie paleolake recorded windier dry seasons in the same way. The similarities in the spectral wavelet analyses of $PC1_{1\text{-}sec}$ and OLO varve thickness support the working hypothesis that the fine laminations in this section of the core are annual.

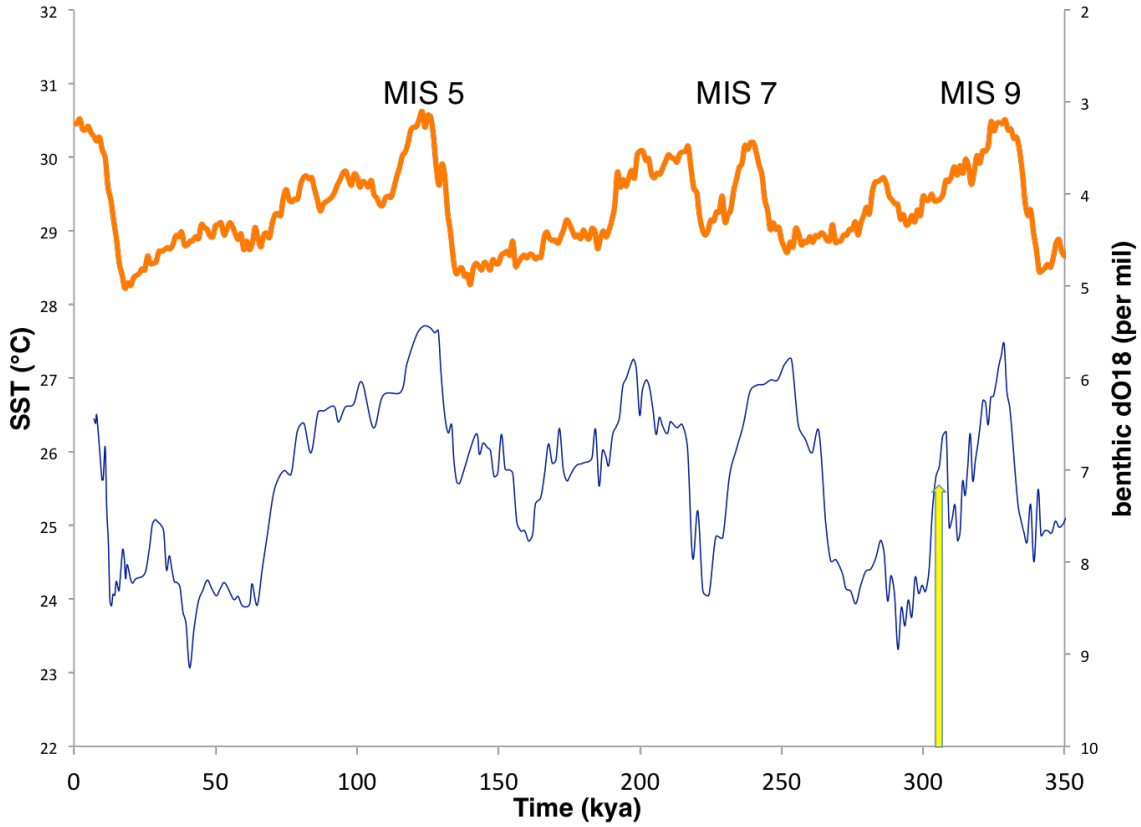

Figure 4.5.1: Tropical SST and dO18 reconstruction
Tropical sea surface temperature reconstruction (blue) from Arabian Sea drill site (core ODP772) (Herbert et. al. 2010), and global dO18 benthic stack with Marine Isotope Stages noted (orange, Lisiecki and Raymo, 2005), approximate age of the finely laminated sediments (320 ka, yellow arrow) noted.

Preliminary Ar/Ar dating places the finely laminated core section at around 320 ka with an uncertainty of +/- 5kyr (Deino personal communication, 2016, Figure 2.3.2). 320 ka was during an interglacial period, as indicated by the Tropical SST temperature reconstruction (Herbert et. al. 2010) and the global

benthic dO18 stack record (Lisiecki and Raymo, 2015, Figure 4.5.1). Even within the error range, it is clear that this deep lake inhabited the Olorgesailie basin during a period with similar temperature as today (Figure 4.5.1). Interaction between the modern ENSO and IOD on East African regional climate is fairly well understood and documented, with the interaction varying more broadly over Holocene records (Sandweiss et al., 2001, Marchant et al. 1999), indicating an even greater variation extending back in geologic history (Marchant 2007). With the relationship between modern IOD and ENSO being fairly contested, it is difficult to conclude what the climate driver is behind the inter-annual signal in the $PC1_{1\text{-}sec}$ and OLO varve thickness data. However, with the similarities in significant frequencies between modern Lake Challa and the Olorgesailie finely laminated sediment suggests the influence of a climate driver that created conditions similar to the modern ENSO/IOD.

5. Conclusions on the Olorgesailie Paleolake Record

The ten core sections of lacustrine sediment analyzed in this research capture a snapshot of varying lacustrine depositional environments in the Olorgesailie basin during a roughly 150 kyr period during the Pleistocene (Deino, personal communication 2016). The three sections that were analyzed further appear to represent three different depositional environments; the banded section characteristic of a shallow alkaline lacustrine environment; the finely laminated section demonstrating a possibly annual record of seasonal changes in a deeper fresher lake, and finally the thinly banded section representing an intermediate lake depth. The paleosols that punctuate the 30m interval that ten lacustrine cores were chosen from, while not part of this research, point to an even more variable depositional environment than just the lake level/alkalinity fluctuations previously discussed. These variable depositional environments in a relatively short section of core show the magnitude of the climate variability during this 150kyr window in the mid-late Pleistocene.

Lake Challa, a modern lake located 240 km from the Olorgesailie basin, has modern varve structure is very similar to the microfacies of the finely laminated section (Wolff 2011). The similarities between the Challa modern sediment and the Olorgesailie finely laminated sediment led to the working hypothesis that the fine laminations in core section 63Q-2 are annual layers. The spectral wavelet analysis performed on $PC1_{1\text{-sec}}$ and the varve thickness data from the finely laminated section of core reveal similar significant frequencies between the two data sets. There is a decadal frequency signal in the $PC1_{1\text{-sec}}$

and varve thickness Olorgesailie data sets that is also evident in the Challa modern varve thickness data. This decadal signal in the OLO core section could be a sedimentary record of a climate driver similar to ENSO or IOD, which has been observed in the modern Lake Challa varves and sediment traps (Wolff 2014, Wolff 2011). The similarities between the finely laminated section's two wavelet analyses and the modern Challa wavelet analysis, coupled with the known similarities in Tropical SSTs between today and 320ka, suggest that the depositional environment of the finely laminated section was similar to the modern Lake Challa.

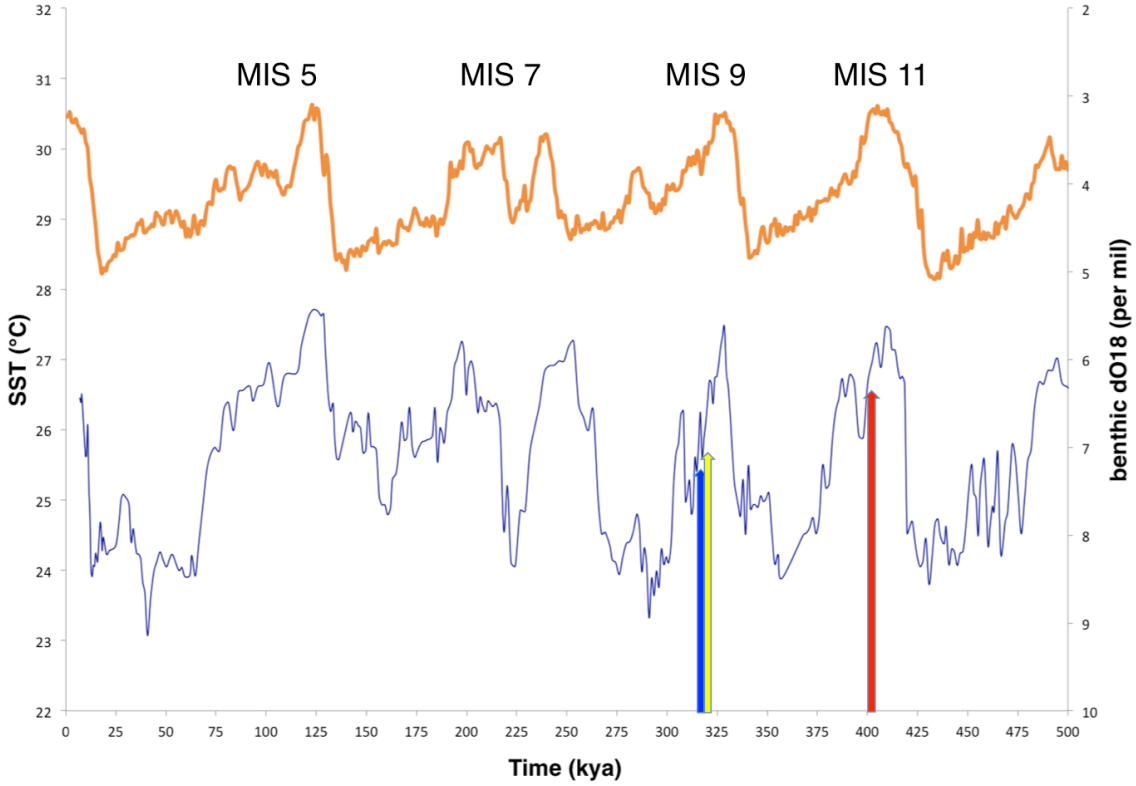

Figure 2.1.1: Tropical SST reconstruction and global benthic dO18 stacked record Tropical sea surface temperature reconstruction (blue) from Arabian Sea drill site (core ODP772) (Herbert et. al. 2010), and global dO18 benthic stack with Marine Isotope Stages noted (orange, Lisiecki and Raymo, 2005). Ar/Ar ages of three core sections noted. The thinly banded section noted with a blue arrow, the finely laminated section noted with a yellow arrow, and the banded section noted with a red arrow.

It is important to note the preliminary nature of the Ar/Ar dates when examining the three cores in context of Pleistocene tropical SSTs (Figure 2.1.1). However, working with the current age model, there is only about 1°C among the three core sections (Figure 2.1.1). This shows that there is very little temperature variation required to dramatically change the climate, and thus depositional environment in the Olorgesailie basin. This is not dissimilar from the research on modern climate change, that only 1°C or 2°C change in global temperature can have a dramatic affect on global climate (IPCC 2014). There are hominin artifacts at the Olorgesailie site that date throughout the middle Pleistocene (Potts 1989,1999). Perhaps the dramatic variability in regional climate recorded in this short lacustrine sequence had an effect on the hominins that also inhabited the Olorgesailie basin during this time. The variability in this short lacustrine interval speaks to the complexities and extreme variability of regional climate and its effect on lacustrine systems.

6. Suggestions for Future Work

Future research on the Olorgesailie drill cores should include comparing this lacustrine sequence with the non-lacustrine sediment that punctuates the 30m section analyzed. Perhaps the intervening non-lacustrine sediment can reveal more about the paleolandscape during this snapshot of the Pleistocene. Once the previous analyses on this drill core have been published and shared, more robust and useful conclusions can be made regarding the paleoclimate at this site and its effect on hominin evolution.

7. References

Brown, E. T., Le Callonnec, L., & German, C. R. 2000, Geochemical cycling of redox-sensitive metals in sediments from Lake Malawi: A diagnostic paleotracer for episodic changes in mixing depth. *Geochimica et Cosmochimica Acta*, *64*(20), 3515–3523. http://doi.org/10.1016/S0016-7037(00)00460-9

Brown, E.T., Johnson, T.C., Scholz, C.A., Cohen, A.S., King, J.W., 2007, Abrupt change in tropical African climate linked to the bipolar seesaw over the past 55,000 years. Geophys. Res. Lett. 34.

Brown, E. T.,Fawcett, P. J., Werne, J. P., Anderson, R. S., Heikoop, J. M., Berke, M. a, … Allen, C. D. 2011, Extended megadroughts in the southwestern United States during Pleistocene interglacials. *Nature*, *470*(7335), 518–521. http://doi.org/10.1038/nature09949

Cohen, A. S., Stone, J. R., Beuning, K. R., Park, L. E., Reinthal, P. N., Dettman, D., ... & Brown, E. T. (2007). Ecological consequences of early Late Pleistocene megadroughts in tropical Africa. *Proceedings of the National Academy of Sciences*, *104*(42), 16422-16427.

Deino, A., Potts, R., 1990. Single-Crystal 40Ar/39Ar dating of the Olorgesailie Formation, southern Kenya rift. JGR 95(B6): 8453-8470

deMenocal, P., 1995. Plio-Pleistocene African climate. Science 270, 53e59.

deMenocal, P., 2004. African climate change and faunal evolution during the Pliocene-Pleistocene. Earth Planet. Sci. Lett. 220, 3e24.

Ebinger, C.J., Yemane, T., Harding, D.J., Tesfaye, S., Kelley, S., Rex, D.C., 2000. Rift deflection, migration, and propagation: linkage of the Ethiopian and Eastern rifts, Africa. GSA Bull. 112, 163e176.

Fetter, C. W. *Applied Hydrogeology*. Upper Saddle River, NJ: Prentice Hall, 2001. Print.

Grootes, P.M., and M. Stuiver. 1997. Oxygen 18/16 variability in Greenland snow and ice with 10^3 to 10^5-year time resolution. Journal of Geophysical Research 102:26455-26470.

Haberzettl, T., Fey, M., Lu, A., Maidana, N., Mayr, C., Ohlendorf, C., … Wille, M. 2005. Climatically induced lake level changes during the last two millennia as reflected in sediments of Laguna Potrok Aike , southern Patagonia, Santa, 283–302.

Han, L. Y., Li, T. Y., Cheng, H., Edwards, R. L., Shen, C. C., Li, H. C., ... & Zhang, T. T. 2015. Potential influence of temperature changes in the Southern Hemisphere on the evolution of the Asian summer monsoon during the last glacial period. *Quaternary International*.

Heath, R. 1983. Basic ground-water hydrology. U.S. Geological Survey Water-Supply Paper 2220. Prepared in cooperation with the North Carolina Department of Natural Resources and Community Development.

Herbert, T.D., L.C. Peterson, K.T. Lawrence, and Z. Liu. 2010. Tropical Ocean Temperatures over the Past 3.5 Myr. Science, Vol. 328, no. 5985, pp. 1530-1534, 18 June 2010. DOI: 10.1126/science.1185435

IPCC, 2014: Climate Change 2014: Synthesis Report. Contribution of Working Groups I, II and III to the Fifth Assessment Report of the Intergovernmental Panel on Climate Change [Core Writing Team, R.K. Pachauri and L.A. Meyer (eds.)]. IPCC, Geneva, Switzerland, 151 pp.

Jones, V. J., Leng, M. J., Solovieva, N., Sloane, H. J., & Tarasov, P. 2004. Holocene climate of the Kola Peninsula; evidence from the oxygen isotope record of diatom silica. *Quaternary Science Reviews*, *23*(7-8), 833–839. http://doi.org/10.1016/j.quascirev.2003.06.014

Katsuta, N., Takano, M., Kawakami, S. I., Togami, S., Fukusawa, H., Kumazawa, M., & Yasuda, Y. 2007. Advanced micro-XRF method to separate sedimentary rhythms and event layers in sediments: its application to

lacustrine sediment from Lake Suigetsu, Japan. *Journal of Paleolimnology*,*37*(2), 259-271.

Kodera, K. 2004. Solar influence on the Indian Ocean monsoon through dynamical processes, Geophys. Res. Lett., 31, L24209, doi:10.1029/2004GL020928.

Kodera, K., Coughlin, K., & Arakawa, O. 2007. Possible modulation of the connection between the Pacific and Indian Ocean variability by the solar cycle. *Geophysical Research Letters*, *34*(3).

Lisiecki, L. E., and M. E. Raymo. 2005. A Pliocene- Pleistocene stack of 57 globally distributed benthic d18O records, Paleoceanography,20, PA1003, doi:10.1029/2004PA001071.

Marchant, M., Hebblen, D. & Wefer, G. 1999. High resolution planktonic foraminiferal record of the last 13,300 years from an up welling area off Chile. Mar. Geol. 161, 115–128.

Marchant, R., Mumbi, C., Behera, S., Yamagata, T., 2007. The Indian Ocean dipole – the unsung driver of climatic variability in East Africa. African Journal of Ecol.

Maslin, M.A., Seidov, D., Lowe, J., 2001. Synthesis of the nature and causes of sudden climate transitions during the Quaternary. In: Seidov, D., Haupt, B.J., Maslin, M. (Eds.), The Oceans and Rapid Climate Change: Past, Present and Future. Am. Geophys. Union Geophys. Monogr. Series, vol. 126. AGU, Washington, DC, pp. 9e52.

Maslin, M. a., & Christensen, B. 2007. Tectonics, orbital forcing, global climate change, and human evolution in Africa: introduction to the African paleoclimate special volume. *Journal of Human Evolution*, *53*(5), 443–464. http://doi.org/10.1016/j.jhevol.2007.06.005

Milankovitch, M.M., 1949. Kanon der Erdbestrahlung und seine Anwendung auf das Eiszeitenproblem. Roy. Serbian Sci., Spec. Pub. 132, Section Mathematical Nat. Sci. 33, Belgrade, 633 pp. (Canon of Insolation and the

Ice Age Problem, English translation by Israel Program for Scientific Translation and published for the U.S. Department of Commerce and the National Science Foundation, Washington, D.C., 1969).

Mohtadi, M., et al., Cooling of the southern high latitudes during the Medieval Period and its effect on ENSO. Quaternary Science Reviews (2007), doi:10.1016/j.quascirev.2006.12.008

Petit, J.R., J. Jouzel, D. Raynaud, N.I. Barkov, J.M. Barnola, I. Basile, M. Bender, J. Chappellaz, J. Davis, G. Delaygue, M. Delmotte, V.M. Kotlyakov, M. Legrand, V. Lipenkov, C. Lorius, L. Pépin, C. Ritz, E. Saltzman, and M. Stievenard. 1999. Climate and atmospheric history of the past 420,000 years from the Vostok Ice Core, Antarctica. Nature 399:429-436.

Pompeani, D. P., B. A. Steinman, and M. B. Abbott. "A sedimentary and geochemical record of water-level changes from Rantin Lake, Yukon, Canada." *Journal of paleolimnology* 48.1 (2012): 147-158.

Potts, R., 1994. Variables vs. models of early Pleistocene hominid land use. J. Hum. Evol. 27:7–24.

Potts, R., 1999. Paleolandscape variation and Early Pleistocene hominid activities: Members 1 and 7, Olorgesailie Formation, Kenya. J. Hum. Evol. 37, 747e788.

Sandweiss, D.H., Maasch, K.A., Burger, R.L., Richardson, J.B., III, Rollins, H.B. & Clement, A. 2001. Variations in Holocene El Nino frequencies: climate records and cultural consequences in ancient Peru. Geology 29, 603-606

Siddall, M., Stocker, T. F., Blunier, T., Spahni, R., Schwander, J., Barnola, J. M., & Chappellaz, J. (2007). Marine Isotope Stage (MIS) 8 millennial variability stratigraphically identical to MIS 3. *Paleoceanography*, *22*(1).

Smith, L.I., 2002. A tutorial on principal components analysis. *Cornell University, USA*, *51*(52), p.65.

Trauth, M.H., Maslin, M., Deino, A., Strecker, M.R., Bergner, A.G.N., Duhnforth, M., 2007. High- and low-latitude forcing of Plio-Pleistocene East African climate and human evolution. J. Hum. Evol. 53, 475e486.

Trauth, M., Maslin, M.A., Deino, A., Strecker, M., 2005. Late Cenozoic mois- ture history of East Africa. Science 309, 2051e2053.

Torrence, C. and Compo, G.P., 1998, A practical guide to wavelet analysis, *Bull. Amer. Meteor. Soc.*, 79, 61-78.

Verschuren, D. 1999. Sedimentation controls on the preservation and time resolution of climate-proxy records from shallow fluctuating lakes, Quaternary Science Reviews, Volume 18, Issue 6, May 1999, Pages 821-837, ISSN 0277-3791

Weber, M.E., Reichelt, L., Kuhn, G., Pfeiffer, M., Korff, B., Thurow, J., and Ricken, W. (2010): The BMPix and PEAK tools: New methods for automated laminae recognition and counting – Application to glacial varves from Antarctic marine sediment. Geochemistry, Geophysics, Geosystems, 11(1), doi:10.1029/2009GC002611

Wolff, C., Haug, G. H., Timmermann, A., Damsté, J. S. S., Brauer, A., Sigman, D. M., ... & Verschuren, D. (2011). Reduced interannual rainfall variability in East Africa during the last ice age. *Science*, *333*(6043), 743-747.

Wolff, C., Kristen-Jenny, I., Schettler, G., Meyer, H., Dulski, P., Naumann, R., Brauer, A., Verschuren, D., Haug, G.H., 2014. Modern seasonality in Lake Challa (Kenya/Tanzania) and its sedimentary documentation in recent lake sediments. Limnol. Oceanogr. 59(5), 2014, 1621-1636.